



# The Lively Accretion Disk in NGC 2992. III. Tentative Evidence of Rapid Ultrafast Outflow Variability

Alfredo Luminari<sup>1,2</sup>, Andrea Marinucci<sup>3</sup>, Stefano Bianchi<sup>4</sup>, Barbara de Marco<sup>5</sup>, Chiara Feruglio<sup>6</sup>, Giorgio Matt<sup>4</sup>, Riccardo Middei<sup>2,7</sup>, Emanuele Nardini<sup>8</sup>, Enrico Piconcelli<sup>2</sup>, Simonetta Puccetti<sup>3</sup>, and Francesco Tombesi<sup>2,9,10,11,12</sup>

<sup>1</sup> INAF—Istituto di Astrofisica e Planetologia Spaziali, Via del Fosso del Cavaliere 100, I-00133 Roma, Italy; [alfredo.luminari@inaf.it](mailto:alfredo.luminari@inaf.it)

<sup>2</sup> INAF—Osservatorio Astronomico di Roma, Via Frascati 33, I-00078 Monte Porzio Catone Roma, Italy

<sup>3</sup> ASI—Italian Space Agency, Via del Politecnico snc, I-00133 Roma, Italy

<sup>4</sup> Dipartimento di Matematica e Fisica, Università degli Studi Roma Tre, via della Vasca Navale 84, I-00146 Roma, Italy

<sup>5</sup> Departament de Física, EEBE, Universitat Politècnica de Catalunya, Av. Eduard Maristany 16, E-08019 Barcelona, Spain

<sup>6</sup> INAF—Osservatorio Astronomico di Trieste, Via G.B. Tiepolo 11 I-34143 Trieste, Italy

<sup>7</sup> Space Science Data Center—ASI, Via del Politecnico s.n.c., I-00133 Roma, Italy

<sup>8</sup> INAF—Osservatorio Astrofisico di Arcetri, Largo Enrico Fermi 5, I-50125 Firenze, Italy

<sup>9</sup> Department of Physics, Tor Vergata University of Rome, Via della Ricerca Scientifica 1, I-00133 Roma, Italy

<sup>10</sup> Department of Astronomy, University of Maryland, College Park, MD 20742, USA

<sup>11</sup> NASA—Goddard Space Flight Center, Code 662, Greenbelt, MD 20771, USA

<sup>12</sup> INFN—Sezione di Roma Tor Vergata, Via della Ricerca Scientifica 1, I-001133 Roma, Italy

Received 2023 February 20; revised 2023 May 1; accepted 2023 May 1; published 2023 June 21

## Abstract

We report on the 2019 XMM-Newton+NuSTAR monitoring campaign of the Seyfert galaxy NGC 2992, observed at one of its highest flux levels in the X-rays. The time-averaged spectra of the two XMM-Newton orbits show ultrafast outflows (UFOs) absorbing structures above 9 keV with  $>3\sigma$  significance. A detailed investigation of the temporal evolution on a  $\sim 5$  ks timescale reveals UFO absorption lines at a confidence level  $>95\%$  ( $2\sigma$ ) in 8 out of 50 XMM-Newton segments, estimated via Monte Carlo simulations. We observe a wind variability corresponding to a length scale of 5 Schwarzschild radii  $r_S$ . Adopting the novel Wind in the Ionized Nuclear Environment model, we estimate the outflowing gas velocity ( $v = 0.21\text{--}0.45c$ ), column density ( $N_H = 4\text{--}8 \times 10^{24} \text{ cm}^{-2}$ ) and ionization state ( $\log(\xi_0/\text{erg cm s}^{-1}) = 3.7\text{--}4.7$ ), taking into account geometrical and special relativity corrections. These parameters lead to instantaneous mass outflow rates of  $\dot{M}_{\text{out}} \simeq 0.3\text{--}0.8 M_\odot \text{ yr}^{-1}$ , with associated outflow momentum rates  $\dot{p}_{\text{out}} \simeq 20\text{--}90 L_{\text{Bol}}/c$  and kinetic energy rates  $\dot{E}_K \simeq 2\text{--}25 L_{\text{Bol}}$ . We estimate a wind duty cycle of  $\approx 12\%$  and a total mechanical power of  $\approx 2$  times the active galactic nuclei (AGN) bolometric luminosity, suggesting that the wind may drive significant feedback effects between the AGN and the host galaxy. Notably, we also provide an estimate for the wind launching radius and density of  $\approx 5r_S$ ,  $10^{11} \text{ cm}^{-3}$ , respectively.

*Unified Astronomy Thesaurus concepts:* X-ray active galactic nuclei (2035); Active galactic nuclei (16); Photoionization (2060)

## 1. Introduction

Variability is one of the best tools to investigate the emission mechanisms at play in active galactic nuclei (AGN). While in many cases significant flux variations can be attributed to variations in the line-of-sight absorbers (e.g., NGC 1365; Risaliti et al. 2005; Walton et al. 2014), some sources have been also observed to vary dramatically in the X-ray intrinsic flux. Recent long XMM-Newton and NuSTAR observations of highly variable sources have led to a number of results that shed light on the accretion/ejection mechanisms in their innermost regions, such as PDS 456 (Nardini et al. 2015; Reeves et al. 2018), IRAS 13349+2438 (Parker et al. 2020), IRAS 13224-3809 (Parker et al. 2017), MCG 03-58-007 (Braitto et al. 2021) and NGC 3783 (Costanzo et al. 2022), among others.

NGC 2992 is a nearby ( $z = 0.00771$ ; Ward et al. 1978; Keel 1996) Seyfert 1.5/1.9 galaxy (Trippe et al. 2008). The large 2–10 keV amplitude variations found in the deep 2005 RXTE monitoring on timescales of days ( $F = 0.8\text{--}8.9 \times$

$10^{-11} \text{ erg cm}^{-2} \text{ s}^{-1}$ ; Murphy et al. 2007) and its high peak brightness make it the ideal case to study the response of the accretion disk to strong changes of the nuclear continuum, via time-resolved spectroscopy. In 2010, NGC 2992 was observed 8 times with XMM-Newton and 3 times with Chandra, with a 2–10 keV flux ranging from  $\sim 5 \times 10^{-12} \text{ erg cm}^{-2} \text{ s}^{-1}$  (its historical minimum) to  $1.5 \times 10^{-11} \text{ erg cm}^{-2} \text{ s}^{-1}$ . A narrow, constant iron line component at 6.4 keV was detected (Murphy et al. 2007; Marinucci et al. 2018). The total iron line equivalent width (EW) and the reflection component are anticorrelated with the flux, suggesting that at least part of them originate from matter rather distant (light years) from the black hole. The source was simultaneously observed with Swift and NuSTAR in 2015 and a 2–10 keV flux of  $5.8 \pm 0.3 \times 10^{-11} \text{ erg cm}^{-2} \text{ s}^{-1}$  was measured. All the past X-ray features of the source were detected (Marinucci et al. 2018): a broad iron K $\alpha$  line (EW =  $250^{+190}_{-120}$  eV), a rather flat intrinsic emission ( $\Gamma = 1.72 \pm 0.03$ , cutoff energy  $E_c > 350$  keV), and a Compton reflection continuum (with a ratio of  $R = 0.18 \pm 0.07$ ). The rise in brightness is accompanied by X-ray spectral features arising from an ultrafast outflow (UFO) with velocity  $v_1 = 0.21 \pm 0.01c$ , one of the few ever detected with NuSTAR alone. The total kinetic energy rate of such a wind is  $\approx 5\% L_{\text{bol}}$ , sufficient to switch on feedback mechanisms

**Table 1**  
Journal of the Observations

| Satellite  | Instrument | Obs. ID     | Net Exposure (ks) | Start Date |
|------------|------------|-------------|-------------------|------------|
| XMM-Newton | pn         | 0840920201  | 92.6              | 2019-05-07 |
| XMM-Newton | pn         | 0840920301  | 92.8              | 2019-05-09 |
| NuSTAR     | FPMA       | 90501623002 | 57.5              | 2019-05-10 |
| NuSTAR     | FPMB       | 90501623002 | 57.1              | 2019-05-10 |

on the host galaxy (Di Matteo et al. 2005; see also Zubovas & Nardini 2020 for the dependence on the wind duty cycle). A reanalysis of the 2003 XMM-Newton bright state confirmed such outflowing absorption structure with an additional wind component detected at  $v_2 = 0.305 \pm 0.005c$ , one of the fastest detected so far in a Seyfert galaxy at an accretion rate of only a few percent of the Eddington value (Tombesi et al. 2010; Gofford et al. 2013).

The Swift-XRT monitoring campaigns (Middei et al. 2022) have been performed between late March and mid-2019 December and 2021 January to December, with a variable interval between the observations: 2 days during the XMM-Newton observing windows and 4 days in the remaining months. Large 2–10 keV amplitude variability was found (ranging between 0.3 and  $1.1 \times 10^{-10}$  erg cm $^{-2}$  s $^{-1}$ ), indicating that the variability timescale is quite short, of the order of days. Simultaneous XMM-Newton (250 ks) and NuSTAR (120 ks) observations were hence triggered on 2019 May 6 (Marinucci et al. 2020, hereafter Paper I). Several iron K emission transients were detected in the 5–7 keV energy band and their location was estimated from fitting 50 EPIC-pn spectra ( $\sim 5$  ks long each). Two components can be ascribed to a flaring emitting region of the accretion disk located at  $\simeq 10\text{--}40 r_g$  from the central black hole ( $r_g = G M_{\text{BH}}/c^2$  is the gravitational radius and  $M_{\text{BH}}$  and  $c$  are the black hole mass and the speed of light, respectively) and one is likely produced at much larger radii ( $> 50 r_g$ ).

We hereby present novel results from the same XMM-Newton and NuSTAR 2019 observations, describing the detection of UFOs and constraining their properties with the novel Wind in the Ionized Nuclear Environment model (WINE), which couples radiative transfer photoionization with a Monte Carlo treatment (Luminari et al. 2018, 2020; Laurenti et al. 2021; Luminari et al. 2021). The paper is structured as follows: in Section 2 we discuss the data analysis procedure and the statistical significance of the UFOs, in Section 3 we apply the WINE model to the most significant spectra, and in Sections 4 and 5 we discuss and summarize our findings.

## 2. Data Analysis

### 2.1. Observations and Data Reduction

NGC 2992 was monitored with Swift-XRT throughout the year 2019 (from March 26 to December 14), to trigger a deep, high-flux XMM-Newton observation of the source. The triggering flux threshold was met on 2019 May 6, with a 2–10 keV flux  $F_{2-10} = 7.0 \pm 0.4 \times 10^{-11}$  erg cm $^{-2}$  s $^{-1}$  (Middei et al. 2022) and XMM-Newton promptly started its 250 ks pointing on the following day, for two consecutive orbits. NuSTAR observed NGC 2992 on 2019 May 10 for 120 ks, simultaneously to the second XMM-Newton orbit, i.e., after  $\sim 185$  ks from the beginning of the pointing. In this paper, we consider the same data set presented in Paper I and we adopt the same binning strategy and nomenclature for each

spectral slice. We report a journal of the observations in Table 1.

For the XMM data, we oversample the instrumental resolution by at least a factor of 3 and require having no less than 30 counts in each background-subtracted spectral channel. The first XMM orbit is divided into bins of 5 ks each, while the second one, together with the NuSTAR observation, in bins of 5.8 ks. Different background regions do not affect the outcomes of the spectral analysis of the XMM-Newton time-averaged spectra, as discussed in Appendix A. NuSTAR spectra are binned in order to oversample the instrumental resolution by at least a factor of 2.5 and to have a signal-to-noise ratio greater than  $3\sigma$  in each spectral channel. We adopt the cosmological parameters  $H_0 = 70$  km s $^{-1}$  Mpc $^{-1}$ ,  $\Omega_\Lambda = 0.73$ , and  $\Omega_m = 0.27$ , i.e., the default ones in XSPEC 12.11.1 (Arnaud 1996). Errors correspond to the 90% confidence level for one interesting parameter ( $\Delta\chi^2 = 2.7$ ), if not stated otherwise.

### 2.2. UFO Detection and Statistical Significance

We fit the time-averaged spectra of the two XMM-Newton orbits between 2 and 12 keV with a model composed of an absorbed power law (ZWABS $\times$ POW in XSPEC) multiplied by a Galactic absorption component (TBABS) with  $N_{\text{H}} \equiv 4.8 \times 10^{20}$  cm $^{-2}$  (Kalberla et al. 2005) and removing the energy range dominated by the Fe K lines (5–8 keV). The ratios between the time-averaged data and the best-fitting continuum models are plotted in Figure 1 (top panel), once the 58 keV band is included, and clear absorption features above 9 keV can be seen. We add to the absorbed power-law baseline model (TBABS $\times$ ZWABS $\times$ POW) five narrow Gaussian lines, of which two reproduce the neutral Fe K $\alpha$  and K $\beta$  and the other three are associated with the  $\sim 5.5$ ,  $\sim 6.7$ , and  $\sim 7.0$  keV transient emission lines, indicated as red flare, blue flare I, and blue flare II, respectively, in Paper I. No strong residuals are present below 9 keV and we obtain best-fit statistics  $\chi^2/\text{dof} = 200/154$  and  $\chi^2/\text{dof} = 216/154$  for the first and second orbit spectra, respectively.

To blindly search for any absorption signature we add an additional Gaussian line left free to vary in the 6–12 keV range, with a normalization that can take both positive and negative values. The Gaussian width is fixed to zero to represent a narrow, unresolved line. We fit the two time-averaged XMM-Newton orbits, leaving the baseline parameters free to vary as well. Figure 1 (bottom panel) shows the corresponding contour plots between the normalization and the line energy centroid. For the first orbit (black data points and contour plots in Figure 1) the inclusion of a Gaussian line leads to a fit improvement of  $\Delta\chi^2 = -18.48$  for two additional degrees of freedom. The best-fit energy of the line is  $11.78^{+0.08}_{-0.15}$  keV, with a normalization  $N = -1.6 \pm 0.6 \times 10^{-5}$  ph cm $^{-2}$  s $^{-1}$ .

To evaluate the statistical significance of narrow, unresolved emission/absorption lines standard likelihood ratio tests could

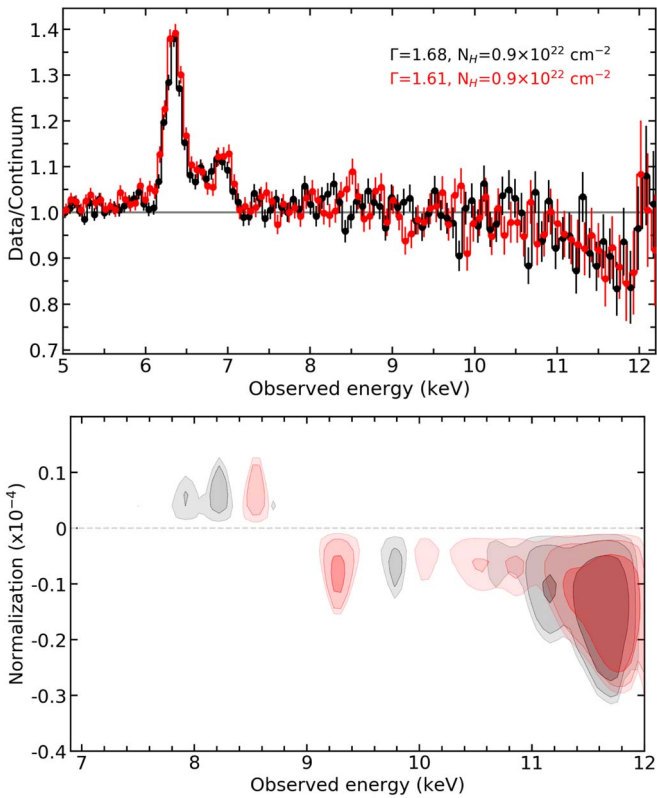


**Figure 1.** Top panel: ratio between the XMM-Newton time-averaged data from the first and second orbit and the associated best-fitting continuum models (black and red lines, respectively). The continuum is composed of an absorbed power law fitted between 35 plus 812 keV; the best-fitting values for the column density and photon index are reported in the top-right corner. Bottom panel: contour plot between the normalization and the observed energy of a variable Gaussian line in the 7–12 keV range. Black and red shaded regions are used for time-averaged spectra from the first and second orbits (darker to lighter colors indicate 99%, 90%, and 68% confidence levels).

lead to inaccurate results (Protassov et al. 2002). Following the procedures described in Tombesi et al. (2010) and Walton et al. (2016), we create Monte Carlo routines to retrieve the statistical significance of the absorption line. We create 10,000 fake data sets of the XMM-Newton EPIC-pn spectrum using the `FAKEIT` command in `XSPEC` with responses, background files, exposure times, and energy binning of the real data according to the following procedure. We first load the best-fitting model, composed of an absorbed power law and five Gaussian lines, and produce a new list of free parameters (i.e., column density of the cold absorber, power-law photon index and normalization, energy, and normalization of the emission lines) by drawing from a multivariate Normal distribution based on the covariance matrix via the `XSPEC` command `TCLOUT SIMPARS`. This allows us to take into account uncertainties in the continuum model, too. Then, this new continuum, without absorption lines and with randomly sampled free parameters, is used to simulate a fake spectrum. Finally, the fake spectrum is fitted, first with the input model (i.e., without absorption lines), and then, including an additional unresolved Gaussian line to the model, with normalization and energy centroid left free to vary in the range  $[-1.0; +1.0] \times 10^{-4}$  ph cm $^{-2}$  s $^{-1}$  and [6:12] keV, respectively. Being  $N$  the number of spectra in which the fit improvement is equal or higher than that of our observed line (i.e.,  $\Delta\chi^2 = -18.48$ ) and  $S$  the total number of simulated spectra, then the estimated statistical significance of the

detection is  $1 - N/S$ . We obtain five spurious detections out of the total 10,000 trials, implying a statistical significance of  $3.5\sigma$ .

We then apply the same procedure to the XMM spectrum of the second orbit (red data points and contour plots in Figure 1). We find two absorption lines at  $9.28 \pm 0.07$  keV, with a normalization  $N = -8.5 \pm 4.0 \times 10^{-6}$  ph cm $^{-2}$  s $^{-1}$  ( $\Delta\chi^2 = -10.18$ ) and at  $11.75 \pm 0.15$  keV, with a normalization  $N = -1.5 \pm 0.6 \times 10^{-5}$  ph cm $^{-2}$  s $^{-1}$  ( $\Delta\chi^2 = -17.65$ ). The significance of these two detections, estimated as above, is  $2.2\sigma$  and  $3.2\sigma$ , respectively. We note that any broadening of such unresolved absorption lines is likely due to the superposition of different spectral features from several time intervals, as we will show in the next sections.

As a further step, we take into account the phenomenological model adopted in Paper I, in which the EPIC-pn spectra from the two orbits (250 ks in total) are divided into 50 bins ranging between 2 and 12 keV. NuSTAR FPMA/B spectra, when available, are simultaneously fitted in the energy interval between 3 and 79 keV. We fit the 50 EPIC-pn spectra leaving the baseline parameters free to vary. Following the same procedure for the blind search of absorption lines described above, we show in Figure 2 the contour plots between the normalization and the energy centroid of the Gaussian line. We adopt the best-fitting models of Paper I, and in addition, we leave the energy centroid of the absorption line free to vary between 6 and 12 keV. We only show the time intervals where we find a detection at a confidence level greater than 99% ( $\Delta\chi^2$  improvement larger than 9.21, for two parameters of interest). The Gaussian width is fixed to 0 keV to represent a narrow, unresolved line. Solid, dashed, and dotted magenta lines indicate 99%, 90%, and 68% confidence levels, corresponding to  $\Delta\chi^2 = -9.21$ ,  $-4.61$ , and  $-2.3$ , respectively. We detect an absorption line at a confidence level greater than 99% in 13 out of 50 spectra (24%). Best-fit values of the baseline parameters are instead fully consistent with the values in Paper I, and thus, we do not report them here. The same procedure is then repeated for the 20 time intervals in which simultaneous EPIC-pn and FPMA/B spectra are available, including cross-calibration constants between the three detectors and leaving the Gaussian energy centroid to vary between 6 and 15 keV. Figure 3 reports the contour plots for the four out of 20 spectra (20%) showing an absorption line with a confidence level  $>99\%$ .

Table 2 reports the best-fitting energies and fluxes of the absorption lines, the  $\Delta\chi^2$  improvement, and the overall  $\chi^2/\nu$  value. For the XMM+NuSTAR spectra corresponding to 220 ks and 278 ks we include also the absorption lines detected with XMM-Newton alone, despite their lower statistical significance (at  $11.24^{+0.12}_{-0.10}$  and  $10.71^{+0.08}_{-0.11}$  keV, respectively). The non-detection of these lines in NuSTAR spectra can be explained in terms of their shorter exposure times and lower spectral resolution at these energies with respect to XMM-Newton. As a consistency check, we fit the unbinned pn spectra together with the FPMA/B spectra with a fixed 200 eV energy binning, leaving the normalization of the lines free to vary between the three detectors and using the Cash statistics (Cash 1976). The inferred normalizations and upper limits are always consistent with each other.

The statistical significance of each detected absorption line listed in Table 2 is then estimated via Monte Carlo simulations, using 1000 fake data sets for each spectrum and the procedure outlined above. We report the inferred significances in Table 2,

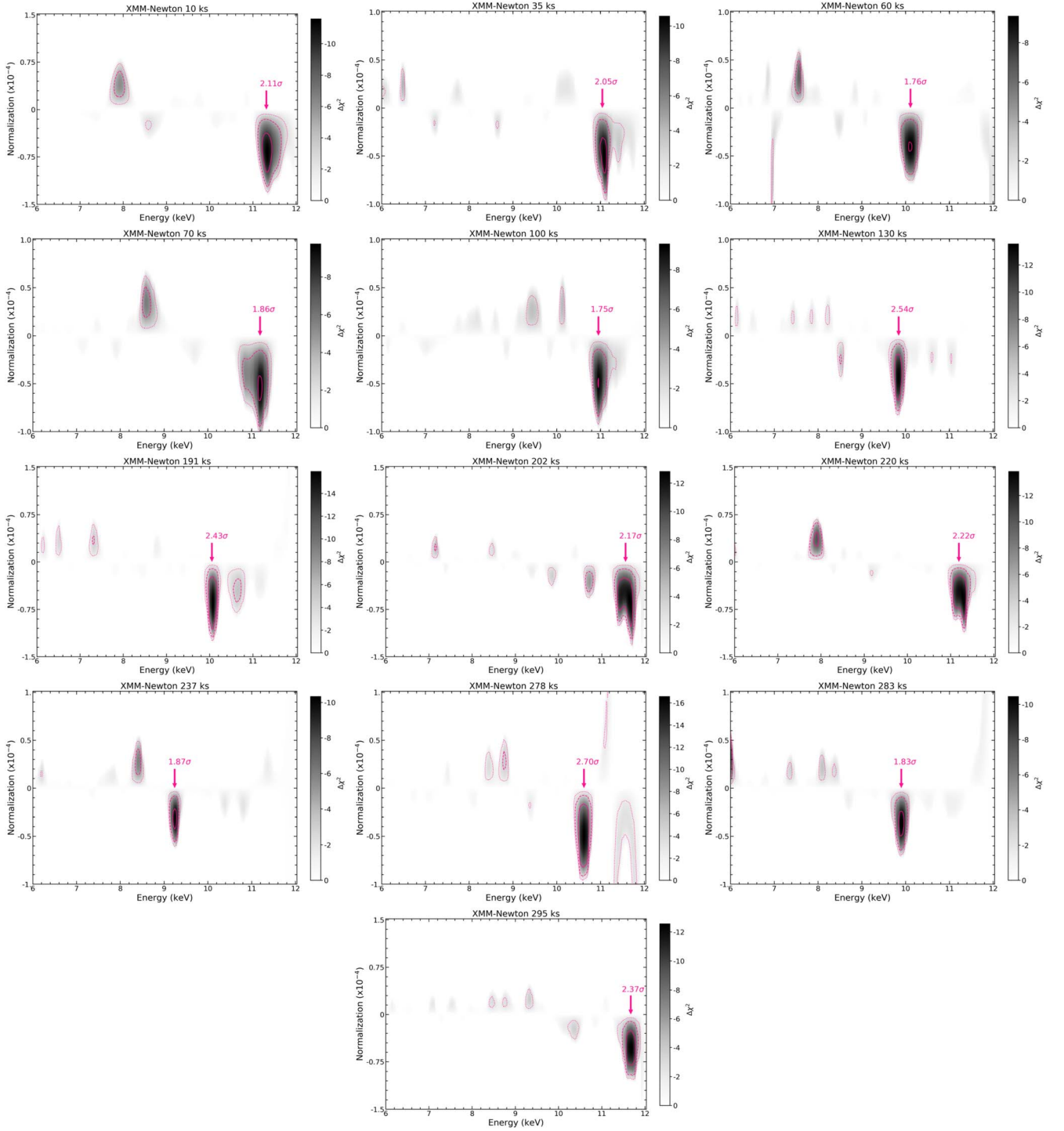


**Figure 2.** XMM-Newton contour plots between the normalization and the observed energy of a variable Gaussian line between 6 and 12 keV. We adopt 200 steps in both normalization and energy and consider a model composed of an absorbed power law and several emission lines, see Section 2.2. Solid, dashed, and dotted magenta lines indicate 99%, 90%, and 68% confidence levels, corresponding to  $\Delta\chi^2 = -9.21, -4.61,$  and  $-2.3,$  respectively. For simplicity, we only show results from time intervals with a  $\Delta\chi^2 < -9.21$ . The significance of the absorption lines, inferred via Monte Carlo simulations, is indicated in magenta.

ranging between  $1.76\sigma$  and  $3.00\sigma$ , in Figures 2 and 3 for the XMM-Newton and joint XMM-Newton+NuSTAR observations, respectively.

We show in the top panels of Figure 4 the eight EPIC-pn spectra with an absorption line with a significance  $>2\sigma$  together with the residuals with respect to a spectral model without and with the absorption line, respectively. Similarly, in the four bottom panels, we show the fits to the joint XMM-Newton+NuSTAR observations with  $>2\sigma$  significance

absorption lines, indicating in red and blue the residuals due to absorption lines in the EPIC-pn and FPMA/B data sets, respectively. For visual clarity, we plot the combined FPMA/B spectra (SETPLOT GROUP command in XSPEC). As a summary of our findings, we plot in Figure 4 (bottom panel) the eight time intervals in which an absorption line is detected on top of the 2–10 keV EPIC-pn light curve.

To estimate the statistical significance of the absorption lines in the global set of spectra, rather than in every single one, we

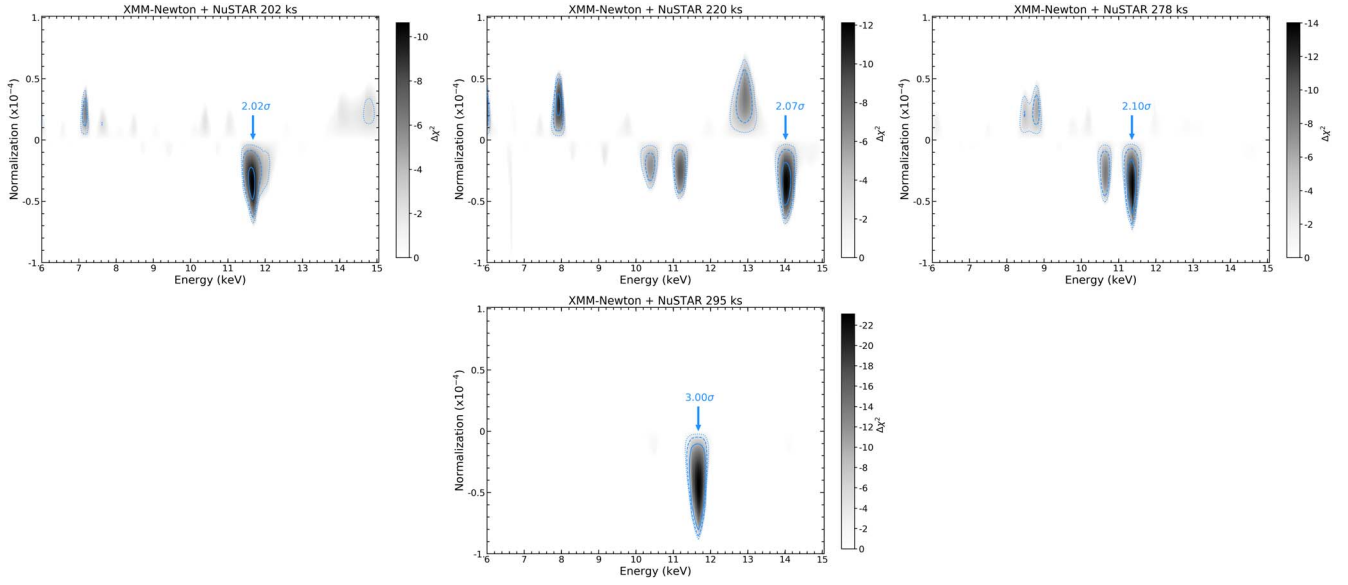


**Figure 3.** XMM-Newton and NuSTAR contour plots between the normalization and the observed energy of a variable Gaussian line between 6 and 15 keV. As in Figure 2 solid, dashed, and dotted light blue lines indicate 99%, 90%, and 68% confidence levels, and we only show results from time intervals with a  $\Delta\chi^2 < -9.21$ . The significance of the absorption lines, inferred via Monte Carlo simulations, is indicated in light blue.

**Table 2**  
Best-fit Parameters of the Time-resolved XMM-Newton and XMM-Newton+NuSTAR Analysis (Top and Bottom Boxes, Respectively)

| Time              | Energy (keV)            | Normalization ( $10^{-5}$ ph cm $^{-2}$ s $^{-1}$ ) | EW (eV)            | $\Delta\chi^2$ | $v_{\text{out}}/c$ (Fe XXV He- $\alpha$ ) | $v_{\text{out}}/c$ (FeXXVI Ly- $\alpha$ ) | MC Sign. $\sigma$ | $\chi^2/\nu$ |
|-------------------|-------------------------|---|--------------------|----------------|---|---|-------------------|--------------|
| XMM-Newton only   |                         |   |                    |                |   |   |                   |              |
| 10 ks             | $11.40^{+0.08}_{-0.10}$ | $-6.5 \pm 3.2$                                      | $-165 \pm 80$      | -11.79         | $0.486^{+0.005}_{-0.007}$                 | $0.456^{+0.005}_{-0.007}$                 | 2.11              | 126/131      |
| 35 ks             | $11.15^{+0.08}_{-0.13}$ | $-5.1 \pm 2.6$                                      | $-155 \pm 80$      | -11.10         | $0.469^{+0.006}_{-0.009}$                 | $0.438^{+0.006}_{-0.009}$                 | 2.05              | 100/123      |
| 60 ks             | $10.15 \pm 0.15$        | $-4.1 \pm 2.1$                                      | $-90 \pm 50$       | -9.62          | $0.39 \pm 0.01$                           | $0.360 \pm 0.013$                         | 1.76              | 119/129      |
| 70 ks             | $11.25^{+0.12}_{-0.10}$ | $-5.6 \pm 2.8$                                      | $-130 \pm 70$      | -10.09         | $0.476^{+0.008}_{-0.007}$                 | $0.446^{+0.008}_{-0.007}$                 | 1.86              | 105/128      |
| 100 ks            | $11.05 \pm 0.10$        | $-5.6 \pm 5.0$                                      | $-130 \pm 70$      | -9.59          | $0.462 \pm 0.007$                         | $0.431 \pm 0.007$                         | 1.75              | 131/126      |
| 130 ks            | $9.90^{+0.07}_{-0.06}$  | $-4.5 \pm 2.0$                                      | $-100 \pm 40$      | -14.40         | $0.372^{+0.006}_{-0.005}$                 | $0.337^{+0.006}_{-0.005}$                 | 2.54              | 137/126      |
| 191 ks            | $10.15 \pm 0.06$        | $-4.3 \pm 1.8$                                      | $-110 \pm 45$      | -15.83         | $0.393 \pm 0.005$                         | $0.359 \pm 0.005$                         | 2.43              | 151/127      |
| 202 ks            | $11.73^{+0.07}_{-0.28}$ | $-6.5 \pm 3.5$                                      | $-220 \pm 120$     | -13.13         | $0.508^{+0.004}_{-0.018}$                 | $0.478^{+0.004}_{-0.019}$                 | 2.17              | 151/125      |
| 220 ks            | $11.35^{+0.07}_{-0.18}$ | $-5.5 \pm 2.7$                                      | $-170 \pm 80$      | -14.15         | $0.483^{+0.005}_{-0.012}$                 | $0.453^{+0.005}_{-0.013}$                 | 2.22              | 107/124      |
| 237 ks            | $9.32^{+0.05}_{-0.08}$  | $-3.1 \pm 1.7$                                      | $-75 \pm 40$       | -10.03         | $0.319^{+0.005}_{-0.008}$                 | $0.283^{+0.005}_{-0.008}$                 | 1.87              | 118/125      |
| 278 ks            | $10.70 \pm 0.08$        | $-4.9 \pm 2.0$                                      | $-125 \pm 55$      | -15.76         | $0.437 \pm 0.006$                         | $0.405 \pm 0.006$                         | 2.70              | 117/128      |
| 283 ks            | $9.96^{+0.10}_{-0.08}$  | $-3.7 \pm 1.8$                                      | $-90 \pm 50$       | -9.94          | $0.377^{+0.008}_{-0.007}$                 | $0.343^{+0.009}_{-0.007}$                 | 1.83              | 122/128      |
| 295 ks            | $11.75^{+0.10}_{-0.11}$ | $-5.4 \pm 2.5$                                      | $-165 \pm 80$      | -12.58         | $0.509^{+0.007}_{-0.006}$                 | $0.480^{+0.007}_{-0.006}$                 | 2.37              | 160/141      |
| XMM-Newton+NuSTAR |                         |   |                    |                |   |   |                   |              |
| 202 ks            | $11.73^{+0.10}_{-0.12}$ | $-3.7 \pm 1.7$                                      | $-130 \pm 60$      | -10.78         | $0.508^{+0.006}_{-0.008}$                 | $0.478^{+0.006}_{-0.008}$                 | 2.02              | 430/375      |
| 220 ks            | $11.24^{+0.12}_{-0.10}$ | $-2.7 \pm 1.4$                                      | $-90 \pm 50$       | -8.48          | $0.476^{+0.008}_{-0.007}$                 | $0.445^{+0.008}_{-0.007}$                 | 2.07              | 384/386      |
|                   | $14.15^{+0.08}_{-0.14}$ | $-3.6 \pm 1.7$                                      | $-170 \pm 80$      | -12.20         | $0.634^{+0.004}_{-0.006}$                 | $0.610^{+0.004}_{-0.006}$                 |                   |              |
| 278 ks            | $10.71^{+0.08}_{-0.11}$ | $-2.7 \pm 1.6$                                      | $-70 \pm 45$       | -8.87          | $0.437^{+0.006}_{-0.008}$                 | $0.405^{+0.006}_{-0.008}$                 | 2.10              | 369/376      |
|                   | $11.46 \pm 0.13$        | $-3.8^{+1.6}_{-1.3}$                                | $-120^{+50}_{-30}$ | -13.19         | $0.490^{+0.008}_{-0.009}$                 | $0.460^{+0.008}_{-0.009}$                 |                   |              |
| 295 ks            | $11.65^{+0.08}_{-0.05}$ | $-4.6 \pm 1.5$                                      | $-150 \pm 50$      | -22.99         | $0.503^{+0.006}_{-0.005}$                 | $0.473^{+0.007}_{-0.005}$                 | 3.00              | 461/409      |

**Note.** Energies are in kiloelectronvolts and in the rest frame of the source ( $z = 0.00771$ ). The statistical significance of each absorption line is determined via Monte Carlo simulations, see the text for details.

simulate the entire set of 50 XMM-Newton time slices via Monte Carlo routines, using the same procedure outlined above. For each time slice we set input parameters drawn from a normal distribution around the best-fit values excluding the Gaussian absorption component. Then, we fit again all the time slices and check how many spurious absorption components

are detected. We simulate the entire set 1000 times and we find that, on average, 2.4 spurious absorption lines are detected at a significance level equal to or higher than our Monte Carlo derived  $2\sigma$  threshold, corresponding to a fit improvement  $\Delta\chi^2 < -11$  (see Table 2). We note that 5 out of 8 detections in the observed spectra have a significance  $\Delta\chi^2 < -13$ , while for

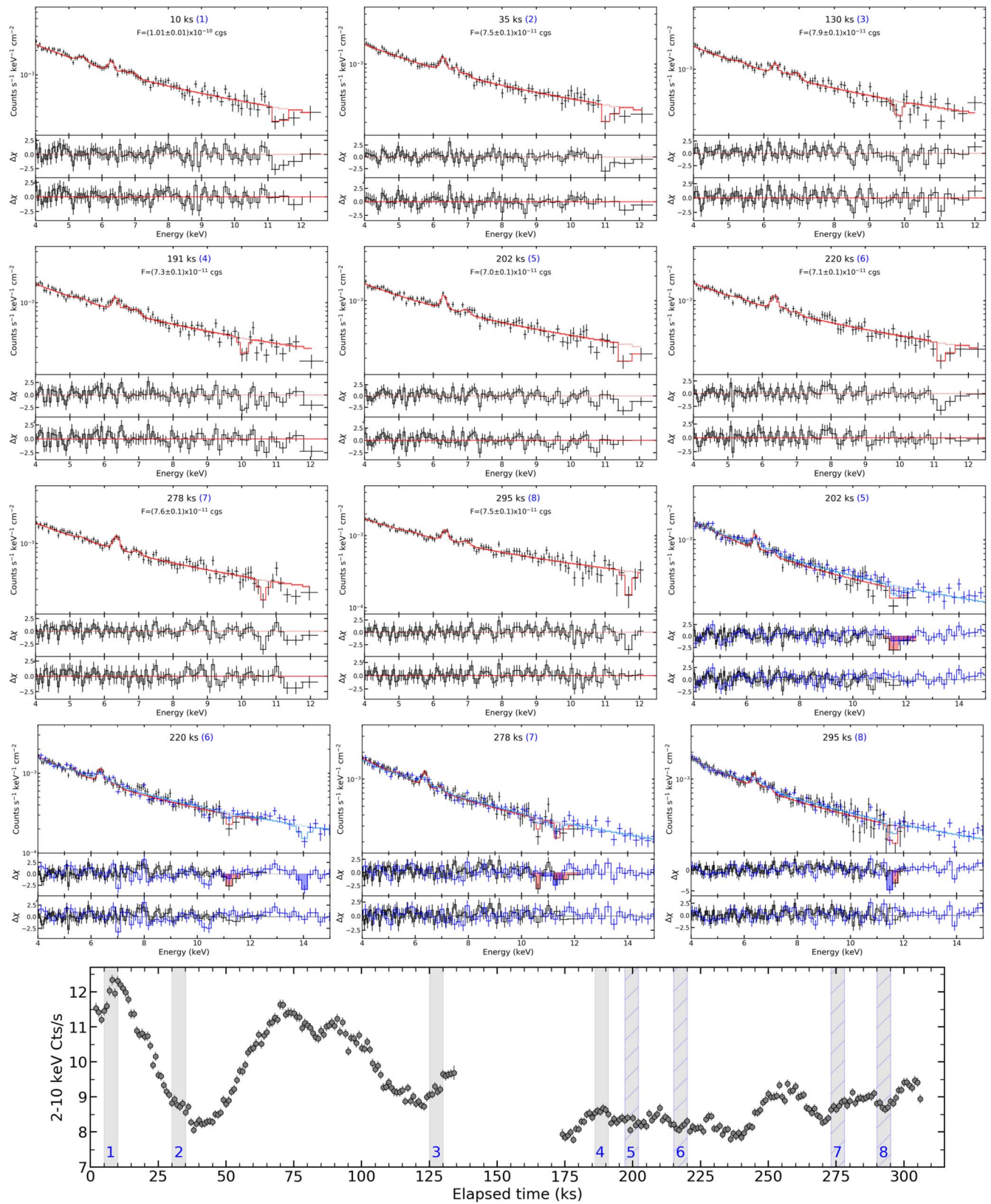


**Figure 4.** From top to bottom and left to right: first seven boxes: top panels show the EPIC-pn spectra with a  $>2\sigma$  significance absorption line. Middle and bottom panels include residuals to a fit using the continuum model and the continuum model plus an absorption line, indicated with dotted and solid red lines, respectively. Last four boxes: EPIC-pn and the combined FPMA/B spectra (black and blue lines) with a  $>2\sigma$  significance absorption line. Bottom panel: 2–10 keV EPIC-pn light curve, with 1 ks time binning. The eight time intervals with  $\sigma > 2$  absorption features are numbered and plotted as gray-shaded regions. Blue stripes indicate the presence of NuSTAR spectra as well.

such significance only 1.2 spurious lines, on average, are detected in the simulated set. Figure 9 (Appendix B) reports the full set of results and the average number of spurious detections for different  $\Delta\chi^2$  thresholds.

Most of the variable absorption lines are detected above 10 keV, an energy range in which the effective area of the EPIC-pn detector significantly decreases. To assess the impact of possible calibration effects we analyze the EPIC-pn spectrum of the Blazar 3C 273, which is well known for showing a simple, featureless continuum (see Appendix A). The spectrum does not show any deviation from a simple power-law continuum or absorption features, further demonstrating that the absorption features in NGC 2992 cannot be ascribed to instrumental effects.

### 3. The WINE Model

#### 3.1. Overview of the Code

To get a complete characterization of the outflow we apply WINE to all the time intervals with UFO signatures detected with a significance  $>2\sigma$ .

WINE is a self-consistent, physically motivated model for wind absorption and emission profiles. Here we provide a brief overview of the model and we refer to Laurenti et al. 2021 and A. L. Luminari et al. 2023, in preparation for a comprehensive description. We represent the wind as a series of thin slabs and we start radiative transfer from the innermost one using the XSTAR photoionization code (Kallman & Bautista 2001) and providing the required parameters, i.e., the inner radius  $r_0$ , the slab column density  $\delta N_{\text{H}}$  and  $\xi_0$ , the ionization parameter at  $r_0$ . The density profile of the wind  $n(r)$  is parameterized through the exponent  $\alpha$  such that  $n(r) = n_0(r_0/r)^\alpha$ , while  $n_0$  can be derived by inverting the definition of the ionization parameter:

$$\xi_0 \equiv L'_{\text{ion}} / (n_0 r_0^2), \quad (1)$$

where  $L'_{\text{ion}}$  is the incident ionizing luminosity in the energy range between 13.6 and 13.6 keV in the gas reference frame, which together with the incident spectrum, is a proxy of the AGN luminosity in XSTAR. Similarly to the density, we implement a power-law behavior for the wind velocity as  $v(r) = v_0(r_0/r)^\zeta$ , where  $\zeta$  is a free parameter of the model. Then, we propagate the simulation to the second slab, using the transmitted spectrum and luminosity as the incident ones and calculating analytically  $\xi$ ,  $r$ ,  $n$ ,  $v$ . We iterate the procedure up to the  $k$ th slab, so that the total wind column density  $N_{\text{H}} = k \cdot \delta N_{\text{H}}$  is reached.

This slicing allows us to reproduce the scaling of the wind properties, including its velocity profile. Given that XSTAR, as well as many other photoionization codes (e.g., Cloudy, Ferland et al. 2017 and SPEX, Kaastra et al. 1996), assumes a null gas outflowing velocity  $v$ , we implemented a procedure to take into account  $v$  in the radiative transfer calculations. This procedure is carried out in a fully special relativity framework and represents a major novelty of WINE. Given the mildly relativistic velocities usually displayed by UFOs, relativistic effects lead to sizeable effects on the appearance of both emission and absorption profiles, which must be properly accounted for to correctly estimate the wind properties, particularly its  $N_{\text{H}}$  (see Luminari et al. 2020 for a detailed description). As a result of these effects,  $L'_{\text{ion}}$  will be in general different (i.e., lower) than the rest-frame measured luminosity,

$L_{\text{ion}}$ . In particular, in the case of a power-law incident spectrum with photon index  $\Gamma$ , the luminosity in the gas frame can be written as  $L'_{\text{ion}} = \left(\frac{1-v}{1+v}\right)^{\frac{2+\Gamma}{2}} \cdot L_{\text{ion}}$ , where  $v$  is in units of  $c$ . Moreover, line emissivities calculated by XSTAR are convolved for each slab with Monte Carlo profiles to accurately represent the wind emission spectrum as a function of its geometry, as well as its ionization, column density, and velocity. This allows us to constrain the presence of wind emission components with higher accuracy with respect to XSTAR or other general-purpose photoionization codes. However, we find that the inclusion of emission features is not statistically supported in any of the time slices, possibly due to a small wind covering factor and/or the limited signal-to-noise ratio of the spectra. For the same reason we do not implement a detailed velocity profile, but we rather set  $\zeta \equiv 0$ , i.e., a constant velocity. As a result, the free parameters of the WINE model, which will then be constrained by fitting the model to the data, are

1.  $\xi_0$ , the ionization parameter at the inner boundary of the wind
2.  $N_{\text{H}}$ , the wind column density
3.  $v_0$ , the outflowing velocity

The remaining free parameters of the model, i.e.,  $r_0$ ,  $\alpha$ , are fixed to  $r_0 = 5 r_{\text{S}}$ ,  $\alpha = 0$ , as explained in Section 3.2. Finally, the AGN ionizing spectral energy distribution (SED) is described through a power law with  $\Gamma = 1.7$  and 2–10 keV luminosity  $L_{2-10} = 1.0 \times 10^{43} \text{ erg s}^{-1}$  (which implies  $L_{\text{ion}} = 2.67 \times 10^{43} \text{ erg s}^{-1}$ ), which are the average values for the time slices analyzed (see Paper I).

#### 3.2. Absorption Tables for NGC 2992

The specific set of XSPEC tables used in this work has been tailored to the (rather extreme) properties of the outflow in NGC 2992. In order to fully understand the behavior of the wind as a function of its  $\xi_0$ ,  $N_{\text{H}}$ ,  $v_0$  it is instructive to examine the wind radial thickness. We define the thickness as  $\Delta_r = \frac{r(N_{\text{H}}) - r_0}{r_0}$ , i.e., the difference between the radius enclosing a column density  $N_{\text{H}}$  and  $r_0$ , normalized by  $r_0$ . According to  $\alpha$ ,  $\Delta_r$  can be written as a function of the initial parameters as follows:

$$\Delta_r = \begin{cases} \left(1 - \frac{N_{\text{H}}}{n_0 r_0 (\alpha - 1)}\right)^{\frac{1}{1-\alpha}} - 1 & \alpha \neq 1 \\ \exp\left(\frac{N_{\text{H}}}{n_0 r_0}\right) - 1 & \alpha = 1 \end{cases}. \quad (2)$$

It can be seen that, as expected,  $\Delta_r$  increases for increasing  $\alpha$ . In particular, for a constant density profile ( $\alpha = 0$ ), the thickness can be written as

$$\begin{aligned} \frac{N_{\text{H}}}{n_0 r_0} &= \frac{N_{\text{H}} \xi_0 r_0}{L'_{\text{ion}}} = \frac{N_{\text{H}} \xi_0 r_0}{\left(\frac{1-\beta}{1+\beta}\right)^{\frac{2+\Gamma}{2}} L_{\text{ion}}} \\ &\approx 2.35 \times 10^{-33} \left(\frac{1+\beta}{1-\beta}\right)^{\frac{2+\Gamma}{2}} N_{\text{H}} \xi_0 r_{0,S} \frac{1}{\lambda_{\text{ion}}} \\ &= 0.17 \left(\frac{1+\beta}{1-\beta}\right)^{\frac{2+\Gamma}{2}} \cdot \frac{N_{\text{H}}}{10^{24}} \cdot \frac{\xi_0}{10^5} \cdot \frac{r_{0,S}}{5}, \end{aligned} \quad (3)$$

where  $L'_{\text{ion}}$  is the relativistic-corrected luminosity in the wind reference frame (see Section 3.1),  $r_{0,S}$  is the launching radius in

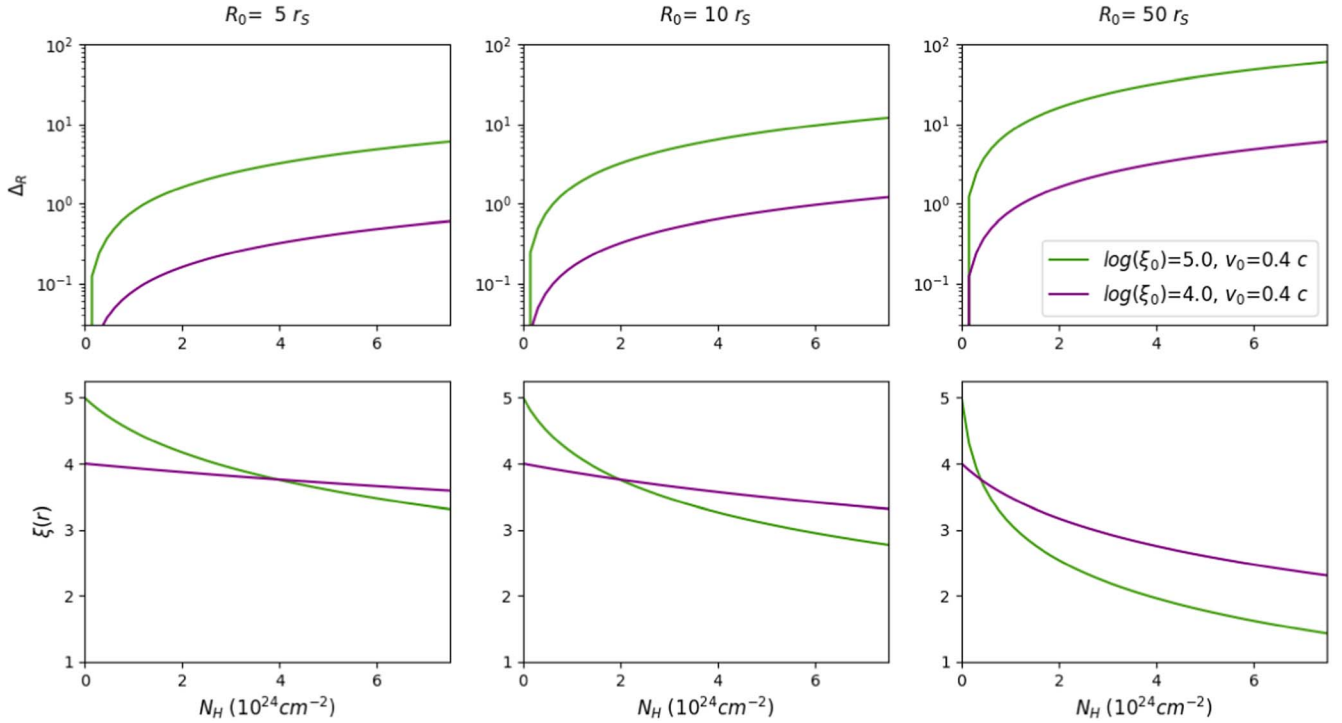


**Figure 5.** Wind radial thickness  $\Delta_r$  (top) and ionization parameter profile  $\xi(r)$  (bottom) as functions of the wind column  $N_{\text{H}}$ , for increasing  $r_0$  (from left to right,  $r_0 = 5, 10, 50r_S$ ).

units of the Schwarzschild radius  $r_S = 2r_g = 2GM_{\text{BH}}/c^2$ ,  $\beta = v_0/c$  and  $N_{\text{H}}$ ,  $\xi_0$  are expressed in units of  $\text{cm}^{-2}$ ,  $\text{erg cm s}^{-1}$ , respectively. In the last step, we assume  $\lambda_{\text{ion}} = 7 \times 10^{-3}$ , as appropriate for NGC 2992 (see Paper I). The relativistic correction is expressed by the term  $\left(\frac{1+\beta}{1-\beta}\right)^{\frac{2+\Gamma}{2}}$ , which for  $v_0 = 0.4c$ ,  $\Gamma = 1.7$  corresponds to 4.8.

In Figure 5 we show  $\Delta_r$  and  $\xi(r)$  (top and bottom panels, respectively) as a function of  $N_{\text{H}}$ , up to  $7.5 \times 10^{24} \text{ cm}^{-2}$ , for  $v_0 = 0.4c$ ,  $\log\left(\frac{\xi_0}{\text{erg cm s}^{-1}}\right) = 4.0, 5.0$ ; these values are representative of those reported in Table 1 and of the best-fit values obtained with WINE (see later). From left to right  $r_0 = 5, 10, 50 r_S$ . The very low normalized luminosity of NGC 2992,  $\lambda_{\text{ion}} = 7 \times 10^{-3}$ , together with the high  $N_{\text{H}}$  and  $v_0$ , contribute to significantly increasing the radial extension of the flow. This, in turn, produces a rapidly decreasing ionization profile through the wind column, due to geometric dilution of the incident radiation flux. As a result, to reproduce the observed high  $\xi$ ,  $N_{\text{H}}$  we need a very low  $r_0$ , of the order of  $5 r_S$ . Although this low value may raise questions about its physical meaning, it must be primarily intended as a numerical strategy to represent a very geometrically thin wind, and thus to minimize the decrease of the ionization parameter and reproduce the high  $\xi_0$  of the observations. We discuss this point further in Section D using the results from the fits described in Section 4.2 below. We also note that the wind properties are variable between one time slice and the following one; the observations have a duration of  $\approx 5$  ks, which can be translated in a dynamical length, for a velocity  $= 0.4c$ , of around  $5 r_S$  (using  $M_{\text{BH}} = 3 \times 10^7 M_{\odot}$ , as estimated in Paper I), in agreement with our  $r_0$ . We also note that an isothermal density profile ( $\alpha = 2$ ), as would be expected for a wind expanding in spherical symmetry, would not be able to reproduce such high column densities, since the maximum value would be limited to

$N_{\text{H}} = 2n_0 r_0 = 2L'_{\text{ion}}/(\xi_0 r_0) = 3.2 \times 10^{24} \text{ cm}^{-2}$  for  $\xi_0 = 10^5 \text{ erg cm s}^{-1}$ ,  $v_0 = 0.4c$ ,  $r_0 = 5r_S$ . The parameter space of the XSPEC tables is as follows:

1.  $N_{\text{H}} = [0.5, 20.0] \cdot 10^{24} \text{ cm}^{-2}$  with a  $0.5 \times 10^{24} \text{ cm}^{-2}$  step
2.  $\log(\xi_0/\text{erg cm s}^{-1}) = [3.00, 6.50]$  with a 0.25 step
3.  $v_0 = [0.15, 0.55] c$  with a  $0.05c$  step

Finally, we tried several values for the turbulent broadening  $\sigma_v$  of the absorption lines. Although the data are weakly sensitive to  $\sigma_v$ , we find that  $\sigma_v = 2500 \text{ km s}^{-1}$  best reproduces the observed lines and we use this value hereafter.

## 4. Results

### 4.1. Time-averaged Spectra

In order to get a zeroth-order characterization of the wind features we first apply WINE to the time-averaged data from the first and second orbit, ranging respectively from 0–125 ks and from 175–300 ks. As before, the energy range is 2–12(3–79) keV for the XMM-Newton(NuSTAR) data sets. The model in XSPEC reads as

$$\text{CONST} \times \text{TBABS} \times (\text{zwabs} \times \text{WINE}_{\text{abs}} \times \text{powerlaw} + 5z\text{gauss})$$

where the constant component (CONST) accounts for the cross-calibration factor between pn and FPMA/B spectra, when present. In order to check the accuracy of WINE we also fit the data using the same model and replacing WINE with XSTAR tables. These tables are built using the same initial conditions (i.e.,  $\sigma_v$ ,  $r_0$ ,  $L_{\text{ion}}$ ,  $\Gamma$ ) and spanning the same parameter range for  $\xi_0$ ,  $N_{\text{H}}$ . Following the standard procedure, we use the XSTAR table redshift as a proxy for the wind velocity, again spanning the same range of velocities as the  $v_0$  parameter in the WINE tables. We report in Table 3 the best-fit values using both WINE and XSTAR. For ease of comparison with the WINE



**Table 3**

Best-fit values for the Time-averaged Spectra, Corresponding to the First XMM-Newton Orbit (Columns 2 and 3) and the Joint Second XMM-Newton Orbit +NuSTAR (Columns 4 and 5)

|   | First Orbit                     |                              | Second Orbit              |                                 |
|---|---------------------------------|------------------------------|---------------------------|---------------------------------|
|   |                                 | ZWABS                        |                           |                                 |
| $N_{\text{H}}$ ( $10^{22}$ cm $^{-2}$ )               | $0.87 \pm 0.04$                 | $0.84 \pm 0.2$               | $1.02 \pm 0.03$           | $1.04 \pm 0.03$                 |
| $\Gamma$  | $1.67 \pm 0.01$                 | $1.663 \pm 0.008$            | $1.655 \pm 0.007$         | $1.658 \pm 0.007$               |
| norm ( $10^{-2}$ )                                    | $2.17 \pm 0.04$                 | $2.15 \pm 0.03$              | $1.81 \pm 0.02$           | $1.82 \pm 0.02$                 |
| $\log\left(\frac{\xi_0}{\text{erg cm s}^{-1}}\right)$ | WINE ABS<br>$4.1_{-0.2}^{+0.6}$ | XSTAR<br>$4.4_{-0.6}^{+0.4}$ | WINE ABS<br>$4.5 \pm 0.4$ | XSTAR<br>$4.02_{-0.08}^{+0.28}$ |
| $v_0$ (c)   | $0.337_{-0.006}^{+0.007}$       | $0.350 \pm 0.006$            | $0.372_{-0.008}^{+0.007}$ | $0.415 \pm 0.006$               |
| $N_{\text{H}}$ ( $10^{24}$ cm $^{-2}$ )               | $3.1 \pm 0.8$                   | $4.0_{-2.5}^{+4.9}$          | $3.8_{-1.6}^{+1.9}$       | $1.2_{-0.4}^{+1.1}$             |
| $\chi^2/\text{dof}$                                   | 190/151                         | 201/151                      | 692/466                   | 707/466                         |

**Note.** Columns 2 and 4 correspond to the fits using WINE, while Columns 3 and 5 to those using XSTAR.

values, we report the relativistically corrected  $N_{\text{H}}$  for XSTAR, obtained by correcting the best-fit column density (and associated error) according to the best-fit redshift-derived velocity (see Luminari et al. 2020 for more details). For each orbit, we obtain a reasonable agreement between the WINE and XSTAR fits, even though the overall fit statistic is better for the WINE fits.

#### 4.2. Time-resolved Spectra

We then apply the same WINE fitting model to the time slices showing absorption lines with a significance  $>2\sigma$  (estimated via Monte Carlo simulations). The analyzed data sets are 10, 35, 130, and 191 ks (XMM-Newton) and 202, 220, 278, and 295 ks (XMM-Newton+NuSTAR). We also include the XMM-Newton coadded spectra corresponding to 60 and 191 ks, since their absorption features have consistent line energy according to the fit in Section 2.2. For the 191 ks observation, we obtain a reduced chi-squared  $\chi^2_{\nu} = 1.14$ , which improves when stacking with the 60 ks one to  $\chi^2_{\nu} = 0.93$ . Best-fit values are consistent between the 191 and the stacked 60 + 191 fit. Table 4 reports the best-fit parameters. We also indicate the wind density  $n_0$ , derived inverting Equation (1) and using the best-fit values for  $\xi_0$ ,  $v_0$ ,  $\Gamma$ , and  $L_{\text{ion}}$ ,  $r_0$  from Section 3. We note that, for a gas in photoionization equilibrium, its ionic population, and thus the emerging spectrum, is mainly determined by the value of  $\xi_0$ . Observationally, once  $L_{\text{ion}}$ ,  $\xi_0$  are measured, it is possible to derive an estimate of  $n_0 r_0^2$ , but the two parameters cannot be disentangled, and thus, they both remain mostly unknown for the majority of UFOs (for further discussion see Nicastro et al. 1999; Krongold et al. 2007; Luminari et al. 2022). However, thanks to our estimate of  $r_0$ , we are able to break this degeneracy, and thus, to provide a value for the wind density. Figure 6 shows the contour plots for all the analyzed time slices, while best-fit spectra and corresponding theoretical model are plotted in Figure 10 in Appendix C, where we also discuss a further absorption line detected in the 220 ks NuSTAR spectrum at  $E \approx 14$  keV. We note that the reduced  $\chi^2$  are similar to those in Table 2, in which absorption features are fitted with Gaussian lines. However, fit statistic shows a significant improvement with respect to the time-averaged WINE fits for the first and second orbits reported in Table 3,

since we are now able to resolve the variable wind features on a 5 ks timescale and analyze them one by one. The averaged spectra are instead 125 ks long and therefore only allow for a characterization of the average wind features.

We verified that a different model component accounting for the neutral absorption along the line of sight (ZTBABS instead of ZWABS) does not affect the best-fitting parameters and the associated statistics.

## 5. Discussion

### 5.1. UFO Energetic and Duty Cycle

The mass outflow rates associated with the UFO features can be calculated through the formula from Crenshaw & Kraemer (2012):

$$\dot{M}_{\text{out}} = 4\pi r_0 N_{\text{H}} \mu m_p C_f v_0, \quad (4)$$

where  $\mu$ ,  $m_p$  are the mean atomic mass per proton (set to 1.2, see Gofford et al. 2015) and the proton mass, respectively, and we set  $r_0 = 5r_S$  following Section 3.2. Due to the weakness of the UFO emission features, we are not able to directly constrain the covering factor  $C_f$  from the observations, so we assume a mean value of 0.4 from the detection occurrence of UFOs in AGN samples (Tombesi et al. 2010; Igo et al. 2020; Matzeu et al. 2022). Then, we calculate the momentum transfer rate as  $\dot{P}_{\text{out}} = \dot{M}_{\text{out}} v_0$  and the kinetic energy according to the special relativity formula as in Laurenti et al. (2021):

$$\dot{E}_{\text{out}} = (\gamma - 1) \cdot \dot{M}_{\text{out}} c^2, \quad (5)$$

where  $\gamma = \frac{1}{\sqrt{1-\beta^2}}$ ,  $\beta = \frac{v_0}{c}$ . We report  $\dot{M}_{\text{out}}$ ,  $\dot{P}_{\text{out}}$ ,  $\dot{E}_{\text{out}}$  for each spectrum in Table 4. Errors are calculated using the standard linear propagation approximation. We do not include the error associated with the black hole mass  $M_{\text{BH}} = 3.0_{-1.5}^{+5.5} \times 10^7 M_{\odot}$ , whose normalized interval (i.e., the error interval divided by the mean value) is higher than those of the WINE parameters reported in Table 4. Including the uncertainty on  $M_{\text{BH}}$  would result in a factor of  $\approx 2$  and  $\approx 4$  increase of the lower and upper bounds of the energetic, respectively. We also note that the commonly used lower limit for  $r_0$ , built from the assumption that  $v_0$  corresponds to the

**Table 4**  
Top: best-Fit Values for the WINE Fits and Derived Number Density of the Wind  $n_0$

| Time Frame (ks)  | 10                     | 35                     | 130                    | 60 + 191                    | 202                    | 220                    | 278                        | 295                  |
|--|------------------------|------------------------|------------------------|-----------------------------|------------------------|------------------------|----------------------------|----------------------|
| $N_{\text{H}}$ ( $10^{22}$ cm $^{-2}$ )                          | $1.1 \pm 0.2$          | $1.0 \pm 0.2$          | $0.8 \pm 0.2$          | ZWABS<br>$0.9 \pm 0.1$      | $1.1 \pm 0.1$          | $1.2 \pm 0.1$          | $1.1 \pm 0.1$              | $1.1 \pm 0.1$        |
| $\Gamma$   | $1.81 \pm 0.04$        | $1.69 \pm 0.06$        | $1.63 \pm 0.06$        | POWERLAW<br>$1.64 \pm 0.04$ | $1.70 \pm 0.03$        | $1.69 \pm 0.03$        | $1.67^{+0.03}_{-0.02}$     | $1.68 \pm 0.03$      |
| norm <sup>a</sup>  | $3.2 \pm 0.2$          | $1.9 \pm 0.2$          | $1.9 \pm 0.2$          | $1.9 \pm 0.1$               | $1.88 \pm 0.09$        | $1.83 \pm 0.09$        | $1.91^{+0.010}_{-0.09}$    | $1.94 \pm 0.09$      |
| $\log\left(\frac{\dot{\epsilon}_0}{\text{erg cm s}^{-1}}\right)$ | $4.6 \pm 0.6$          | $4.2^{+0.7}_{-0.4}$    | $4.7^{+0.4}_{-0.6}$    | WINE ABS<br>$3.75 \pm 0.2$  | $4.5^{+0.3}_{-0.5}$    | $4.7^{+0.5}_{-0.8}$    | $>4.5$ (6.5) <sup>b</sup>  | $4.5^{+0.3}_{-0.4}$  |
| $v_0$ (c)  | $0.45^{+0.03}_{-0.02}$ | $0.32^{+0.02}_{-0.03}$ | $0.21^{+0.01}_{-0.03}$ | $0.37 \pm 0.01$             | $0.35^{+0.03}_{-0.02}$ | $0.27^{+0.02}_{-0.03}$ | $0.43^{+0.02}_{-0.01}$     | $0.35 \pm 0.01$      |
| $N_{\text{H}}$ ( $10^{24}$ cm $^{-2}$ )                          | $8.2^{+2.8}_{-2.7}$    | $7.8^{+4.2}_{-3.2}$    | $6.6^{+4.8}_{-3.3}$    | $5.1^{+3.8}_{-2.3}$         | $4.0^{+2.7}_{-2.3}$    | $5.1^{+2.9}_{-2.0}$    | $5.9^{+2.9}_{-2.0}$        | $5.8^{+1.8}_{-2.3}$  |
| $\log\left(\frac{n_0}{\text{cm}^{-3}}\right)$                    | $10.7 \pm 0.6$         | $11.35^{+0.4}_{-0.7}$  | $11.0^{+0.6}_{-0.4}$   | $11.8 \pm 0.2$              | $11.0^{+0.5}_{-0.3}$   | $11.0^{+0.8}_{-0.5}$   | $<10.9$ (8.9) <sup>b</sup> | $11.0^{+0.4}_{-0.3}$ |
| $\chi^2/\text{dof}$  | 126/135                | 102/127                | 131/130                | 177/190                     | 432/379                | 399/392                | 378/382                    | 448/401              |
| $\dot{M}_{\text{out}}$<br>( $10^{25}$ g s $^{-1}$ )              | $5.0^{+1.7}_{-1.6}$    | $3.3^{+1.8}_{-2.2}$    | $1.9^{+1.4}_{-1.0}$    | $2.5^{+1.9}_{-1.1}$         | $1.9^{+1.7}_{-1.3}$    | $1.8^{+1.0}_{-1.5}$    | $3.4^{+1.7}_{-1.2}$        | $2.8^{+0.9}_{-1.2}$  |
| $\dot{p}_{\text{out}}$<br>( $10^{35}$ g cm s $^{-2}$ )           | $6.7^{+2.4}_{-2.3}$    | $3.2^{+1.7}_{-2.1}$    | $1.2^{+0.9}_{-0.6}$    | $2.7^{+2.1}_{-1.2}$         | $2.0^{+1.2}_{-1.4}$    | $1.5^{+0.8}_{-1.2}$    | $4.4^{+2.2}_{-1.5}$        | $2.9^{+0.9}_{-1.2}$  |
| $\dot{E}_{\text{out}}$<br>( $10^{45}$ erg s $^{-1}$ )            | $5.3^{+2.0}_{-1.8}$    | $1.6^{+0.9}_{-1.1}$    | $0.4^{+0.3}_{-0.2}$    | $1.7^{+1.3}_{-0.8}$         | $1.2^{+0.7}_{-0.8}$    | $0.6^{+0.3}_{-0.5}$    | $3.3^{+1.6}_{-1.1}$        | $1.7^{+0.6}_{-0.7}$  |
| $\dot{M}_{\text{out}}$ ( $M_{\odot}$ yr $^{-1}$ )                | $0.8 \pm 0.3$          | $0.5 \pm 0.3$          | $0.3^{+0.2}_{-0.1}$    | $0.4^{+0.3}_{-0.2}$         | $0.3 \pm 0.2$          | $0.3^{+0.1}_{-0.2}$    | $0.5^{+0.3}_{-0.2}$        | $0.4^{+0.1}_{-0.2}$  |
| $\dot{p}_{\text{out}}$ ( $L_{\text{bol}}/c$ )                    | $89^{+32}_{-30}$       | $62^{+33}_{-41}$       | $20^{+15}_{-11}$       | $51^{+38}_{-23}$            | $37^{+23}_{-26}$       | $28^{+15}_{-23}$       | $77^{+38}_{-26}$           | $51^{+16}_{-22}$     |
| $\dot{E}_{\text{out}}$ ( $L_{\text{bol}}$ )                      | $23.5^{+8.9}_{-8.1}$   | $10.6^{+5.8}_{-7.3}$   | $2.2^{+1.6}_{-1.3}$    | $10.3^{+7.7}_{-4.7}$        | $7.2^{+4.6}_{-5.1}$    | $3.9^{+2.1}_{-3.3}$    | $19.0^{+9.5}_{-6.6}$       | $9.8^{+3.3}_{-4.2}$  |

**Note.** Bottom: mass, momentum, and energy transfer rates (see Section 5), both in cgs and normalized units. Errors are reported at the 90% c.i. (a) In units of  $10^{-2}$  ph. keV $^{-1}$  cm $^{-2}$  s $^{-1}$  at 1 keV. (b) Values in parentheses indicate the upper/lower bounds. The  $1\sigma$  best-fit values are  $\log\left(\frac{\dot{\epsilon}_0}{\text{erg cm s}^{-1}}\right) = 5.2^{+0.8}_{-0.3}$ ,  $\log\left(\frac{n_0}{\text{cm}^{-3}}\right) = 10.1^{+0.3}_{-0.8}$ .

escape velocity of the flow, is equal to  $r_{\text{min}} = 4.9^{+0.4}_{-0.7}$ ,  $22.3^{+6.5}_{-2.2} r_{\text{S}}$  for the fastest and slowest velocities reported in Table 4, i.e.,  $v_0 = 0.45, 0.21c$ ; using these values would result in generally higher values of the energetic, which linearly scales with  $r_0$  (see Equation (4)).

Interestingly, the fact that  $r_{\text{min}} \geq r_0$  implies that the detected UFO velocities are always lower than the escape ones; therefore, the wind will need additional acceleration, e.g., through radiation or magnetocentrifugal forces (e.g., Blandford & Payne 1982; Proga et al. 2000; Cui & Yuan 2020, but see Section 6 for further discussion), in order to overcome the gravitational force of the central black hole. In case of insufficient acceleration, the outflow may turn into a so-called *failed wind*, which is ubiquitously expected in all the radiative driving scenarios as a result of the over-ionization of the gas closer to the black hole (Higginbottom et al. 2014; Dannen et al. 2019), and in turn, is fundamental for the shielding of the outer gas layers (see Zappacosta et al. 2020 and references therein). Given the short distance from the black hole, this outflow may also be linked to the dynamics of the X-ray corona, whose physical dimension is supposed to vary according to accretion rate variations (see, e.g., Kara et al. 2019; Alston et al. 2020); as discussed in Section 1 and 5.3, NGC 2992 is indeed a strongly variable source.

Our derived values for the energetic are extremely high with respect to the typical UFO ones reported in the literature; as an example,  $\dot{E}_{\text{out}}$  is usually found to be around 0.1–1 times  $L_{\text{bol}}$  (see, e.g., Fiore et al. 2017), while here it is in the range of 2–23  $L_{\text{bol}}$ . This is due to the very high values found for  $v_0, N_{\text{H}}$ , i.e.,  $\sim 0.3c$ ,  $6 \times 10^{24}$  cm $^{-2}$ , making NGC 2992 an outlier with

respect to the nearby Seyferts, which typically show  $v \sim 0.1c$ ,  $N_{\text{H}} \sim 10^{23}$  cm $^{-2}$  (see, e.g., Tombesi et al. 2011). We note that, as a result of the high observed velocities, the relativistic reduction of the gas opacity (and then, of its observed column density) is particularly significant. This, together with the lower collecting area of XMM-Newton above 10 keV, makes the features with low  $N_{\text{H}}$  more difficult to detect, possibly resulting in a bias in our analysis toward high  $N_{\text{H}}$ , and in turn, in an underestimate of the wind activity. This bias may explain, at least partly, the high column densities reported in Table 4 with respect to the Tombesi et al. (2011) mean values. Moreover, as we will discuss below, NGC 2992 shows evidence of a *changing-look* activity, hinting at differences in the accretion-ejection dynamics with respect to *canonical* Seyfert galaxies. Interestingly, UFOs detected in quasars show higher  $v_0, N_{\text{H}}$  with respect to Seyfert galaxies; as an example, Chartas et al. (2021) concentrate on a sample of quasars at  $1.4 \leq z \leq 3.9$ , finding an average  $v_0 \approx 0.3c$  and  $N_{\text{H}} \approx 4 \times 10^{23}$  cm $^{-2}$  (which, once relativistically corrected for  $0.3c$ , corresponds to  $N_{\text{H}}^{\text{rel}} \sim 8 \times 10^{23}$  cm $^{-2}$ ). Nardini et al. (2015) and Tombesi et al. (2015) both found similar  $v_0 \approx 0.25c$ ,  $N_{\text{H}}^{\text{rel}} \approx 1.2 \times 10^{24}$  cm $^{-2}$  for the UFOs in PDS 456 ( $z = 0.184$ ) and in IRAS F1119+3257 ( $z = 0.189$ ), respectively.

Thanks to our time-resolved analysis we are able to estimate the duty cycle of the wind, i.e., the fraction of time during which it is observed. Considering that the amount of spurious detection within the full set of time slices amounts to  $\approx 2$  for our  $2\sigma$  significance threshold (see Section 2.2 and Appendix B), we can conservatively assume that at least six of the XMM-Newton UFO detections (out of a total of eight) are not due to noise fluctuations. For a total of 50 time slices,

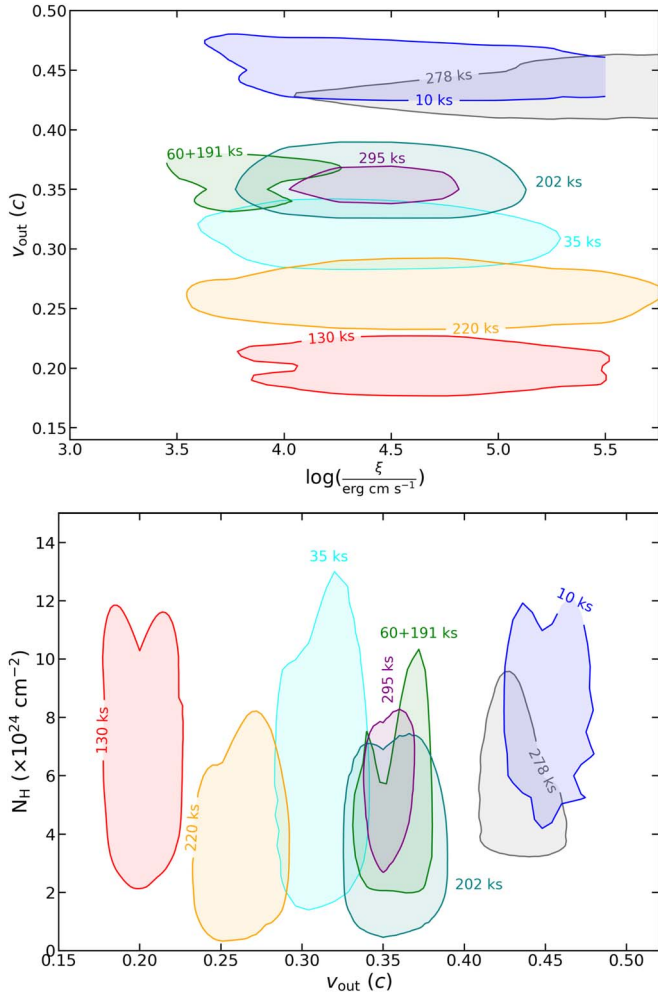


**Figure 6.** Contour plots between the outflowing velocity of the gas and the ionization parameter and between the column density and the outflowing velocity (top and bottom panel, respectively) obtained with WINE, for the eight analyzed spectral intervals. For visual clarity, we only show curves corresponding to a 90% confidence level.

this translates into a lower limit for the duty cycle of  $6/50 = 12\%$ . However, we caution that the observing bias discussed above may likely result in an underestimate of the duty cycle. We can derive mass and energy outflow rates representative of the total observing time as the average of the values reported in Table 4 times the wind duty cycle, thus obtaining  $\dot{M}_{\text{out}}^{\text{tot}} = 0.05 M_{\odot} \text{ yr}^{-1}$ ,  $\dot{E}_{\text{out}}^{\text{tot}} = 1.3 L_{\text{bol}}$ . We also note that, from a historical point of view, UFO features have been detected in high-flux observations only, which however occurred only  $\approx 30\%$  of the time from the first X-ray observation of NGC 2992 in 1978 (Marinucci et al. 2018). Thus, the inferred duty cycle may not be regarded as representative of the global AGN lifetime.

UFO features were already detected in Marinucci et al. (2018) in two high-flux observations of NGC 2992, the 2003 XMM-Newton and the joint 2015 NuSTAR+Swift one, with 2–10 keV luminosities  $L_{2-10} = 1.3 \times 10^{43}$ ,  $7.6 \times 10^{42} \text{ erg s}^{-1}$ , respectively, comparable to that of our 2019 observations,  $L_{2-10} = 1.0 \times 10^{43} \text{ erg s}^{-1}$ . Our derived values for  $\dot{M}_{\text{out}}$ ,  $\dot{E}_{\text{out}}$  are a factor  $> 10$  higher than those reported in Marinucci et al. (2018) due to the different wind properties: our best-fit values for  $N_{\text{H}}$ ,  $v_{\text{out}}$  are in the range of  $4\text{--}8 \times 10^{24} \text{ cm}^{-2}$  and  $0.2\text{--}0.4c$ , while in 2003(2015) observations they found

$N_{\text{H}} = 2.2 \times 10^{23} (1.8 \times 10^{22}) \text{ cm}^{-2}$  and  $v_0 \approx 0.2\text{--}0.3c$ . We note that neglecting the relativistic reduction of the wind opacity would have led to a 35%–55% lower  $N_{\text{H}}$  (according to our range of  $v_0$ ) with respect to the WINE-derived value. As an additional consistency check, we fit again the 2003 XMM-Newton observations using the same fitting model of Marinucci et al. (2018) and replacing the original wind tables, computed with the Cloudy code (Ferland et al. 2017), with our WINE tables. We obtain best-fit values consistent with those in Marinucci et al. (2018) and significantly lower than the present ones, further confirming the robustness of WINE when compared to different codes on one side, and on the other, the peculiarity of the wind features reported in this paper with respect to the archival ones. The high column densities inferred for the 2019 data set, easily exceeding the Compton-thickness threshold, suggest a scenario in which the observed features can be ascribed to independent, high-velocity clouds ejected from the disk, possibly embedded in a much lower  $N_{\text{H}}$  wind. We discuss such a scenario in the next subsection.

### 5.2. UFO Energetic According to the Cloud Scenario

Equation (4) is calculated under the assumption of a spherical symmetric flow (Crenshaw et al. 2003; Crenshaw & Kraemer 2012), as commonly assumed for UFOs (see e.g., Tombesi et al. 2012; Nardini et al. 2015; Fiore et al. 2017; Chartas et al. 2021). However, the outflow in NGC 2992 shows a very low duty cycle and a short-term variation of its spectral appearance, equal to or lower than the 5 ks timescale of our observations. Moreover, we do not detect any emission feature associated with the UFO; therefore, we are not able to put constraints on its angular extension. Therefore, we also consider a complementary scenario, dubbed *cloud scenario* in which the UFO absorption features are due to outflowing (spherical) gas clouds passing through our line of sight for a time  $t \approx 5 \text{ ks}$  (see Bianchi et al. 2009 for a similar approach). For each time slice we derive the mass and energy outflows as follows. We compute the average radial distance of each cloud as

$$r_{\text{avg}} = r_0 + r(N_{\text{H}}/2) = r_0 + \frac{N_{\text{H}}/2}{n_0}, \quad (6)$$

where  $r(N_{\text{H}}/2)$  is the radius enclosing half of the wind column density and the last term is valid for a constant density wind ( $\alpha = 0$ , see Equation (2)). Then, assuming that the cloud is rotating at a distance  $r_{\text{avg}}$  from the black hole with a Keplerian velocity  $v_{\text{rot}}$ , its dimension  $D$  can be estimated as  $D = t \cdot v_{\text{rot}} = t \cdot \sqrt{GM_{\text{BH}}/r_{\text{avg}}}$ , where  $t = 5 \text{ ks}$ . Finally, the mass of the cloud is given by

$$M_{\text{out}} = \frac{4}{3} \pi (D/2)^3 n_0. \quad (7)$$

We report  $M_{\text{out}}$  in Table 5, together with the associated energy  $E_{\text{out}} = (\gamma - 1) M_{\text{out}} c^2$ , where now we use the composition between outflowing and rotational velocity, i.e.,  $\beta_{+} = \sqrt{v_{\text{rot}}^2 + v_0^2} / c$ . We also calculate the average mass and energy rates as the ratio between the sum of  $M_{\text{out}}$ ,  $E_{\text{out}}$  for all the observations divided by the total observing time, i.e., 250 ks. With respect to  $\dot{M}_{\text{out}}^{\text{tot}}$ ,  $\dot{E}_{\text{out}}^{\text{tot}}$  computed assuming spherical symmetry, we obtain lower values by a factor of  $\approx 100$  and 2, respectively. Given the large number of assumptions, in

**Table 5**  
Energetic According to the Cloud Scenario

| Time Frame (ks) | $M_{\text{out}}$<br>( $10^{-6}M_{\odot}$ )                | $E_{\text{out}}$<br>( $10^{47}$ erg)       |  |
|-----------------|---|--|--|
| 10              | 0.65  | 1.71                                       |  |
| 35              | 7.55  | 13.46                                      |  |
| 130             | 2.71  | 2.75                                       |  |
| 60 + 191        | 27.7  | 67.6                                       |  |
| 202             | 3.61  | 7.35                                       |  |
| 220             | 2.82  | 3.78                                       |  |
| 278             | 0.06  | 0.12                                       |  |
| 295             | 3.06  | 5.94                                       |  |
| Total           | 48.2  | 102.7                                      |  |
|                 | $\dot{M}_{\text{out}}$<br>( $M_{\odot} \text{ yr}^{-1}$ ) | $\dot{E}_{\text{out}}$<br>(erg s $^{-1}$ ) | $\dot{L}_{\text{bol}}$<br>( $L_{\text{bol}}$ ) |
| Time avg.       | $6.08 \times 10^{-3}$                                     | $4.11 \times 10^{43}$                      | 0.23   |

**Note.** From top to bottom we report  $M_{\text{out}}$  and  $E_{\text{out}}$  (left to right) for the single observations and their sum. The last row shows the average mass and energy rates for the total observing time.

Table 5 we only report the mean values, with the aim of demonstrating the importance of a proper description of the UFO geometry and dynamic for a reliable estimate of its energetic.

### 5.3. Connection with the Accretion Disk

We are not able to find any correlation among the UFO parameters and between these and the properties of the continuum spectrum (e.g., photon index, normalization), both for the present and the Marinucci et al. (2018) observations. However, we note that the 2003 and 2015 UFO features were also accompanied by a broad component of the Fe K $\alpha$  emission line, while instead both the wind and the emission are absent in the low-flux XMM-Newton observations from 2010–2013, which have  $L_{2-10} < 4 \times 10^{42}$  erg s $^{-1}$ .

By analyzing all the optical and X-ray observations from 1978 up to 2021, Guolo et al. (2021) found evidence for a *changing-look* behavior of NGC 2992, which appears to be driven primarily by the intrinsic luminosity (i.e., the accretion rate), rather than by obscuration or transient events such as TDEs. Their main finding supporting this interpretation is the anti-correlation between  $L_{2-10}$  and the FWHM of the H $\alpha$  line; moreover, they also found a positive correlation between  $L_{2-10}$  and (i) the flux of the Fe K $\alpha$  line and (ii) the flux of the H $\alpha$  line in the optical band. H $\beta$  line was also detected, albeit with a lower confidence, for the brightest observations, showing a fairly constant H $\alpha$ /H $\beta$  flux ratio of  $\sim 9$ . The luminosity threshold for the appearance of the H $\alpha$  line is  $2.6 \times 10^{42}$  erg s $^{-1}$ , corresponding to an Eddington ratio of  $\approx 1\%$ . Interestingly, they suggest the possibility that, due to the low accretion rate, the accretion disk could be thin, pressure dominated at large radii (as in the standard Shakura & Sunyaev 1973 picture) and radiatively inefficient in the innermost regions (Yuan & Narayan 2014), and the high-luminosity intervals are associated with instabilities at the boundary between these two regimes. UFOs have been always observed in high-luminosity states; unless this evidence is entirely due to the low constraining power of the low-flux spectra, it represents an indication of a link between the

radiative efficiency of the inner region and the ejection of matter in the form of relativistic disk winds.

## 6. Conclusions

In this paper, we analyze the UFO absorption features, at energies  $E \gtrsim 9$  keV, detected in the 2019 XMM-Newton +NuSTAR monitoring campaign of the Seyfert galaxy NGC 2992. The time-averaged spectra show absorption lines at a significance  $>3\sigma$ , estimated via a set of 1000 Monte Carlo simulations. Moreover, the high flux of these observations allows us to perform a time-resolved spectroscopic analysis of the absorption features with a temporal resolution of  $\sim 5$  ks. We obtain a Monte Carlo-derived significance  $>2\sigma$  for four time slices of the first XMM-Newton orbit and four of the joint XMM-Newton+NuSTAR observations.

We fit these spectra with the novel photoionization and spectroscopic model WINE (Luminari et al. 2018, 2020; Laurenti et al. 2021, A. L. Luminari et al. 2023, in preparation), which self-consistently calculates wind absorption and emission profiles using a realistic, physically motivated dynamical and geometrical representation of the outflows for AGN and compact sources (Section 3). Notably, WINE also includes the special relativity effects on the gas opacity (as discussed in Luminari et al. 2020), which are particularly important given the high detected velocities, between  $v_0 = 0.21$  and  $0.45c$ , resulting in an increase of the intrinsic wind column  $N_{\text{H}}$  with respect to the observed (i.e., apparent) one by a factor between 35% and 55%, respectively.

Our main findings can be summarized as follows:

1. We detect fast, massive, and ionized outflows, with average  $v_0 = 0.35c$ ,  $N_{\text{H}} = 5.8 \times 10^{24}$  cm $^{-2}$ ,  $\log\left(\frac{\xi_0}{\text{erg cm s}^{-1}}\right) = 4.5$ . Notably, these values are far higher than those typically found for UFOs in nearby Seyfert galaxies and resemble those observed in highly accreting quasars. On the basis of geometrical and dynamical considerations, we suggest the wind is launched from a short distance to the black hole, of the order of  $5 r_{\text{S}}$ . Interestingly, this value is in rough agreement with the dynamical length obtained as the product between the timescale of the UFO appearance ( $\approx 5$  ks) and a typical flow velocity of  $0.4c$ . Through  $r_0$ ,  $\xi_0$  we are also able to provide an estimate of the wind density  $n_0 \approx 10^{11}$  cm $^{-3}$ . We estimate a UFO duty cycle of  $\approx 12\%$  as the fraction of time slices in which we obtained a detection with a  $>2\sigma$  significance of the corresponding absorption features, corrected by the possible contribution from noise fluctuations. However, this value likely represents a lower limit, since both relativistic effects and the limited XMM-Newton effective area above 10 keV may result in a lower detection rate of the features with lower  $N_{\text{H}}$ . The wind best-fit values of the time-averaged spectra are consistent with the time-resolved ones, further confirming the robustness of our analysis.
2. The *instantaneous* momentum outflow rate,  $\dot{p}_{\text{out}}$ , for the analyzed time slices lies in the range  $20\text{--}89L_{\text{bol}}/c$ , strongly suggesting the presence of additional launching mechanisms at work beside radiation pressure, such as magnetohydrodynamic (MHD) acceleration, especially given the low bolometric luminosity during these observations, around 4% the Eddington value (Fukumura et al. 2010; Gaspari & Sadowski 2017; Cui & Yuan 2020; Luminari et al. 2021).  $\dot{p}_{\text{out}}$  has been computed assuming a

spherical symmetric outflow, as usually done for UFOs (see Equation (4)); similarly, we compute instantaneous mass and energy outflow rates, of the order of  $\dot{M}_{\text{out}} \approx 0.5M_{\odot} \text{ yr}^{-1}$ ,  $\dot{E}_{\text{out}} \approx 10L_{\text{bol}}$ , respectively.

Using the wind duty cycle we are able to derive *average* mass and energy outflow rates representative of the total observing time, i.e.,  $\dot{M}_{\text{out}}^{\text{tot}} = 0.05M_{\odot} \text{ yr}^{-1}$ ,  $\dot{E}_{\text{out}}^{\text{tot}} = 1.3L_{\text{bol}}$ . The energy outflow rate is of the same order as the theoretical threshold (between 0.5% and 5%  $L_{\text{bol}}$ , Di Matteo et al. 2005; Hopkins & Elvis 2010) required to switch on feedback effects in the host galaxy. However, we caution that the low accretion rate of the central black hole will probably prevent the nuclear wind to develop a fully energy-conserving Galactic outflow (see, e.g., Faucher-Giguère & Quataert 2012; King & Pounds 2015; Torrey et al. 2020); therefore, we only expect a moderate outflow activity in the host galaxy.

We also caution that for an MHD-driven wind, the conservation of angular momentum implies  $\dot{M}_{\text{in}} = (r_A/r_0)^2 \dot{M}_{\text{out}}$ , where  $\dot{M}_{\text{in}}$  is the rate of accreting mass and  $r_A/r_0$  is the ratio between the Alfvén and the launching radii of the wind. Such a ratio is usually estimated in the interval 1–10 (see e.g., Pudritz et al. 2007; Cui & Yuan 2020; Fiore et al. 2023), thus predicting  $\dot{M}_{\text{out}} = 0.1\text{--}1\dot{M}_{\text{in}}$ . Our instantaneous mass outflow rates are  $\approx 10\text{--}20\dot{M}_{\text{in}}$ , and therefore, in tension with the MHD prediction. Such high rates would remove more angular momentum than that of the accreting mass, leading to accretion *bursts*, and thus, significant X-ray variability, as indeed observed in NGC 2992 (see Section 1). The average mass outflow rate is  $\dot{M}_{\text{out}}^{\text{tot}} \approx 1.7\dot{M}_{\text{in}}$ , possibly indicating a longer-term equilibrium between accretion and ejection. However, additional observations of NGC 2992 are needed to carefully investigate this hypothesis.

3. We propose the alternative scenario in which the UFOs are associated with a series of clouds passing through our line of sight with a 5 ks timescale. The associated mass and energy rates,  $\approx 6 \times 10^{-3}M_{\odot} \text{ yr}^{-1}$ ,  $0.2L_{\text{bol}}$  respectively, are significantly lower than the above ones. Even though we are not able to provide precise measurements due to the large number of assumptions, this exercise demonstrates the importance of a proper physical setting when calculating the wind energetic.
4. Disk winds have been observed in NGC 2992 only in three high-luminosity observations, i.e., the 2019 campaign analyzed here and two previous observations from 2003 and 2015 (Marinucci et al. 2018), where also a broad Fe  $K\alpha$  emission line was present. Interestingly, all these observations caught the source with a luminosity above the threshold of  $L_{2-10} = 2.6 \times 10^{42} \text{ erg s}^{-1}$  (corresponding to 1%  $L_{\text{Edd}}$ ) identified by Guolo et al. (2021), over which broad H $\alpha$  and H $\beta$  lines are detected in the optical band. This evidence may suggest a link between the accretion disk activity and the presence of UFOs.
5. Outflows in the optical band have been observed from the broad line region up to galactic scales by several authors (Veilleux et al. 2001; Irwin et al. 2017; Mingozzi et al. 2019; Guolo-Pereira et al. 2021), suggesting a link between nuclear and galactic scales. A forthcoming paper (Zanchettin et al., submitted) will analyze further ALMA and MUSE observations probing the complex interplay

between the different gas phases (cold molecular, warm ionized, and the radio jet), in order to investigate the relation between AGN, winds, jet, and the Galactic disk.

This is the third paper of a series devoted to the 2019 observation campaign of NGC 2992, after Marinucci et al. 2020; Middei et al. 2022. As a further step, we plan to apply WINE to the 2003 and 2015 high-flux observations in order to build a homogeneous census of the UFO features in NGC 2992 and assess in detail the relation between disk winds and accretion disk.

### Acknowledgments

We thank the referee for their valuable and interesting comments. A.M., S.B., G.M., E.N., E.P., and S.P. acknowledge support from the PRIN MIUR project “black hole winds and the Baryon Life Cycle of Galaxies: the stone-guest at the galaxy evolution supper,” contract No. 2017PH3WAT. A.L. acknowledges support from the HORIZON-2020 grant “Integrated Activities for the High Energy Astrophysics Domain” (AHEAD-2020), G.A. 871158. B.D.M. acknowledges support via a Ramn y Cajal Fellowship (RYC2018-025950-I), the Spanish MINECO grant PID2020-117252GB-I00, and the AGAUR/Generalitat de Catalunya grant SGR-386/2021. R.M. acknowledges the financial support of INAF (Istituto Nazionale di Astrofisica), Osservatorio Astronomico di Roma, ASI (Agenzia Spaziale Italiana) under contract to INAF: ASI 2014-049-R.0 dedicated to SSC. S.B., E.P. acknowledge financial support from ASI under grants ASI-INAF I/037/12/1 and n. 2017-14-H.O. We used ASTROPY, a community-developed core PYTHON package for Astronomy (Astropy Collaboration et al. 2013, 2018), NUMPY (Harris et al. 2020), and MATPLOTLIB (Hunter 2007). This research has made use of the NuSTAR Data Analysis Software (NuSTARDAS) jointly developed by the ASI Science Data Center (ASDC, Italy) and the California Institute of Technology (USA).

### Appendix A

#### EPIC-pn Background and Calibration

The 2019 flux levels of the source were remarkably high compared to previous observations (Murphy et al. 2007). However, the observed background can still be relevant above 10 keV, where the EPIC-pn effective area has a significant drop. In this Appendix, we try different extraction regions for the time-averaged background spectra of the two XMM orbits and compare them with the ones used throughout our previous analysis. Figure 7 (left panels) shows the three circular regions (with 50'' radii) from which spectra are extracted. Red circles indicate the background regions used in Section 2.2. In the 10–12.5 keV energy band, the flux of the background is 3.7% and 7.9% of the source flux for the first and second orbit, respectively. No significant statistical variations are found in the best-fit values and in the overall  $\chi^2/\text{dof}$  for the time-averaged spectra when using the three different background regions.

As an additional test, we reduced the XMM-Newton pn data set for the Blazar 3C 273, which is well known for showing a smooth broadband continuum at hard X-ray energies (Madsen et al. 2015). The observation was performed on 2018 July in Small Window Mode (ObsID 0414191401), i.e., less than a year before our observations of NGC 2992 and with the same operational settings. The 3C 273 data are not affected by background flares and have a net

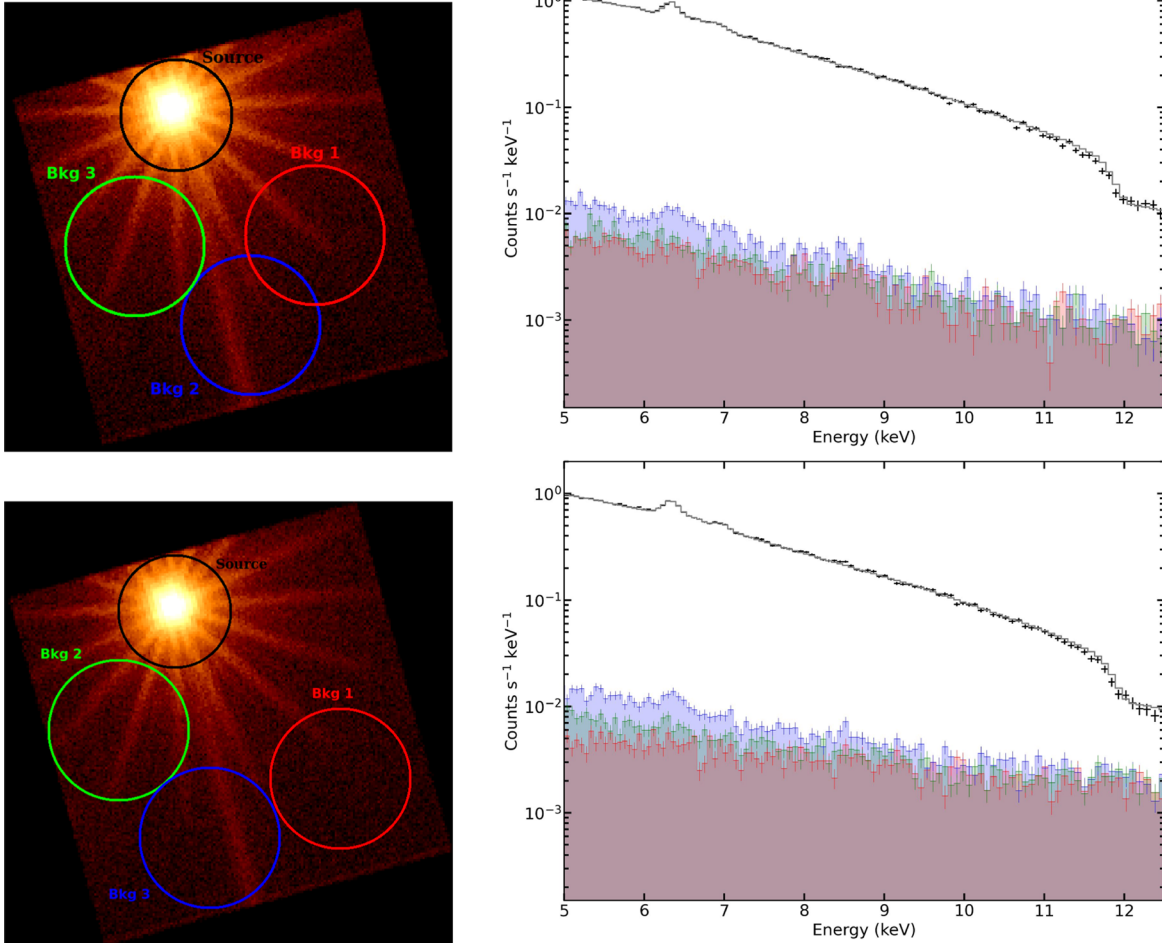


**Figure 7.** Left panels: EPIC-pn filtered event files for orbits 1 (top) and 2 (down). The source spectrum is a circular region with  $40''$  radius, while different circular regions with  $50''$  radii are tested as background regions. Right panels: time-averaged spectra, in black, for orbit 1 (92.6 ks long, top figure) and 2 (92.8 ks long, bottom figure). Shaded regions indicate different background spectra; red ones correspond to those used throughout the paper. Best-fit models are shown as gray solid lines.

exposure time of 44.3 ks. The flux level of the source ( $F_{2-10} = 6 \times 10^{-11} \text{ erg cm}^{-2} \text{ s}^{-1}$ ) is comparable with that of NGC 2992 during the second orbit. The extracted spectrum is shown in Figure 8 with its best-fit power law over the range 5–12 keV ( $\Gamma = 1.70$ ) and the relative residuals (bottom panel). It is worth noting that the spectrum of 3C 273 does not show any deviation from a simple power law up to 12 keV (compare with Figure 1 for NGC 2992), implying that there are no calibration issues above 10 keV and that the

ancillary response files of the EPIC-pn detector are fully reliable in this spectral region in spite of the drop of the effective area. We replaced the 3C 273 pn background with the NGC 2992 one, we modeled the continuum with an absorbed power law, and applied the same blind scan of Section 2.2 to search for absorption lines in the 6–12 keV energy range. No absorption lines are detected at the 99% c. l., further demonstrating that the lines detected in the NGC 2992 observations are not due to background artifacts.

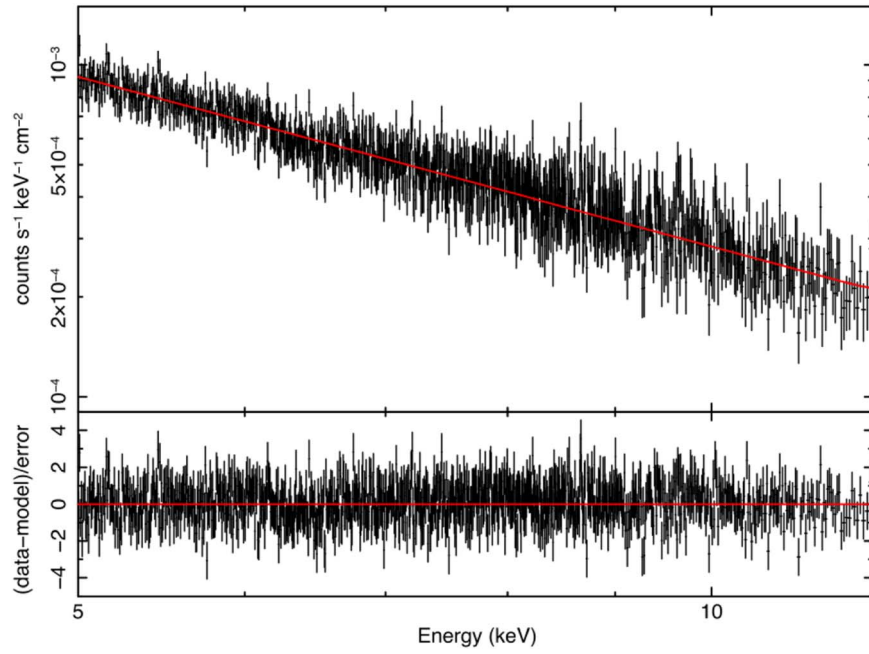


**Figure 8.** The EPIC-pn spectrum of 3C 273 and its best-fit power law (top) and the associated residuals (bottom).

### Appendix B Monte Carlo Simulations

Figure 9 reports the results of the 1000 Monte Carlo simulations of the entire set of 50 XMM-Newton time slices. From left to right and top to bottom, each panel reports, for

increasing significance, the distribution of the spurious Gaussian absorption components detected in each set. Each distribution is fitted with a Gaussian profile to derive its mean  $\mu$  and standard deviation  $\sigma$ , which are reported on top of each plot. The mean number of spurious detections ranges from  $\mu = 4.9$  for  $\Delta\chi^2 < -9$  to  $0.9$  for  $\Delta\chi^2 < -14$ .

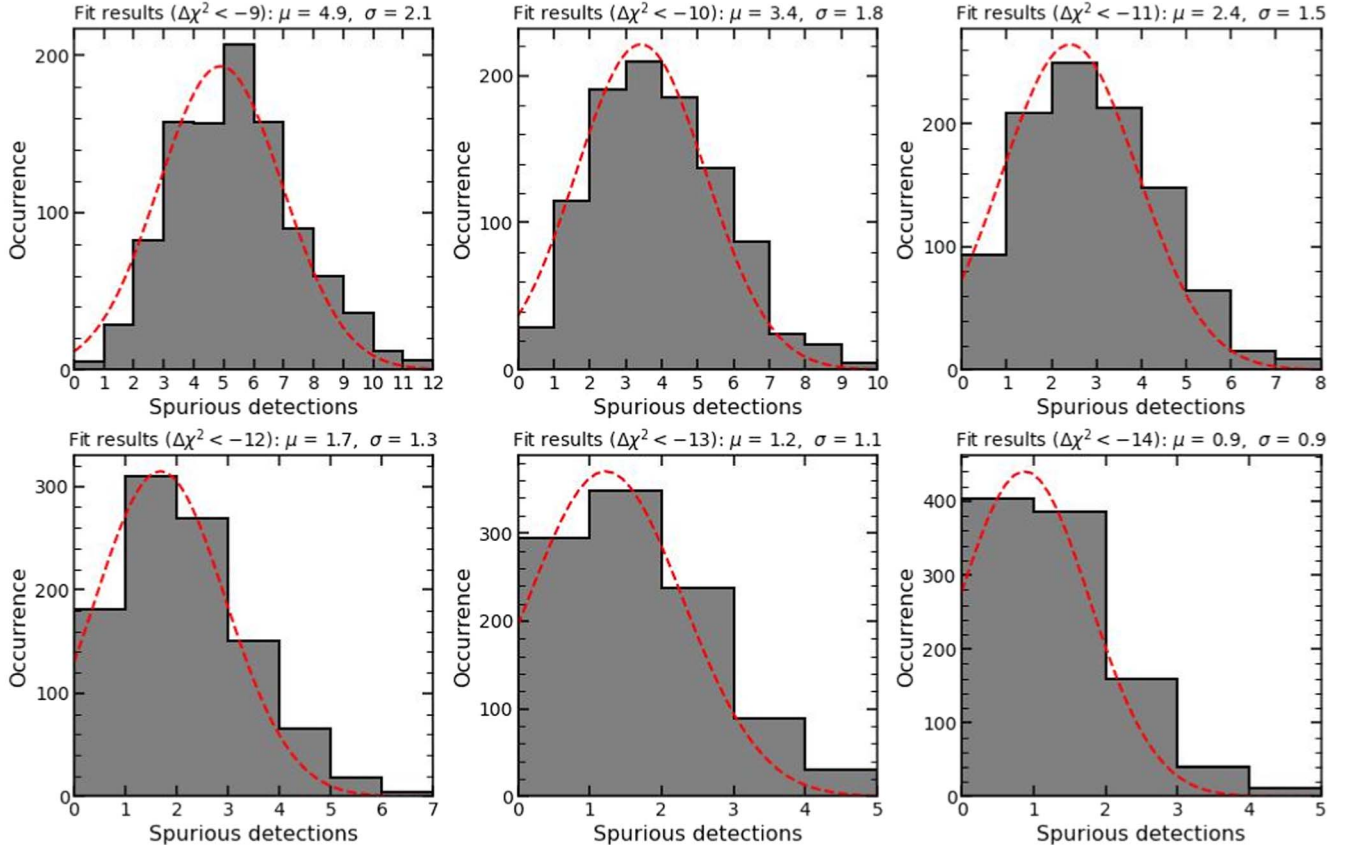


**Figure 9.** Histograms of the absorption lines detected in the 1000 simulated data sets. Red dashed lines represent the corresponding best-fit Gaussian distributions, whose mean  $\mu$  and standard deviation  $\sigma$  are reported on the top of each box. From left to right and top to bottom the statistical threshold increases (from  $\Delta\chi^2 < -9$  to  $< -14$ ).

### Appendix C WINE Best Fits

Figure 10 shows the best fits obtained with WINE. For each time slice, we show the data sets and the best-fit model, folded with the instrumental response (top), the residuals (middle), and the (unfolded) best-fit model (bottom). Dotted lines indicate the Gaussian lines associated with the accretion disk emission (see Section 2.2).

We note that the  $E \approx 14$  keV absorption line detected by NuSTAR in the 220 ks spectrum, with a Monte Carlo-estimated significance of  $2.07\sigma$  (see Table 2), would imply an outflow velocity  $\sim 0.62c$  if ascribed to Fe XXV He $\alpha$  or FeXXVI Ly $\alpha$ .

We try to fit this line with WINE using an updated set of tables, spanning velocities up to  $v_0 = 0.70c$ . However, we are not able to reproduce such a feature within our model, since for such high velocities the radial thickness  $\Delta_r$  dramatically increases, and as a result, the ionization parameter  $\xi(r)$  strongly decreases along the wind column due to the geometric dilution of the ionizing flux. For comparison, we show in Figure 11 a plot of  $\Delta_r$ ,  $\xi(r)$  (top and bottom panels, respectively) for the best-fit values of the 220 ks observation,  $\log\left(\frac{\xi_0}{\text{erg cm s}^{-1}}\right) = 4.7$ ,  $v_0 = 0.27c$  (purple line, see Table 4), together with a solution with same  $\xi_0$  but  $v_0 = 0.62c$ , where the effects of the higher velocity are clearly visible.

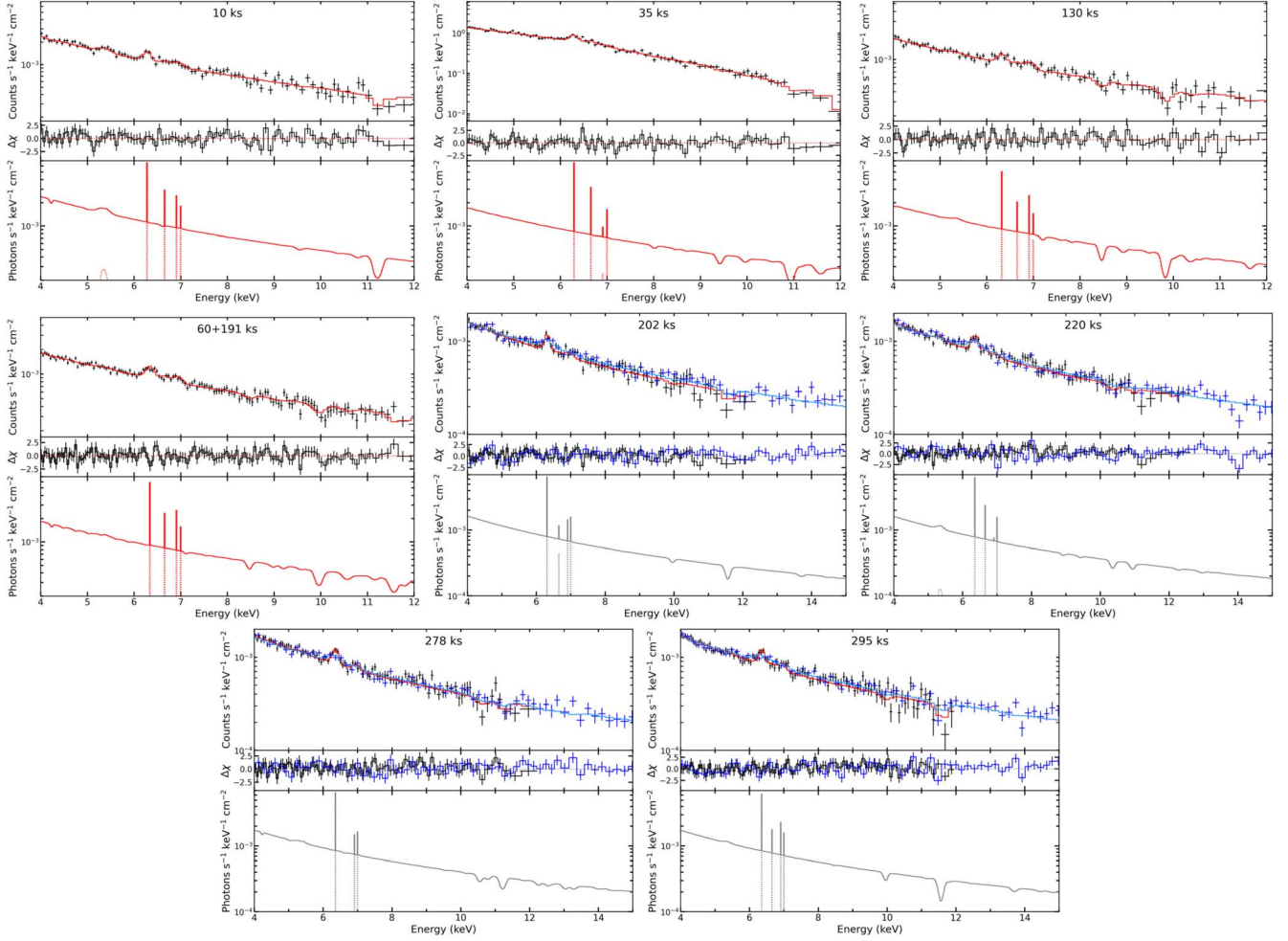


**Figure 10.** Each box reports the best fit and the model for the observations fitted with WINE. Top panels: spectrum and best-fit model, folded with the instrument response. Middle panels: residuals in units of  $\chi^2$ . Bottom panels: best-fit model (unfolded). Data points are plotted in black(blue) and models in red(light blue) for XMM-Newton (NuSTAR).



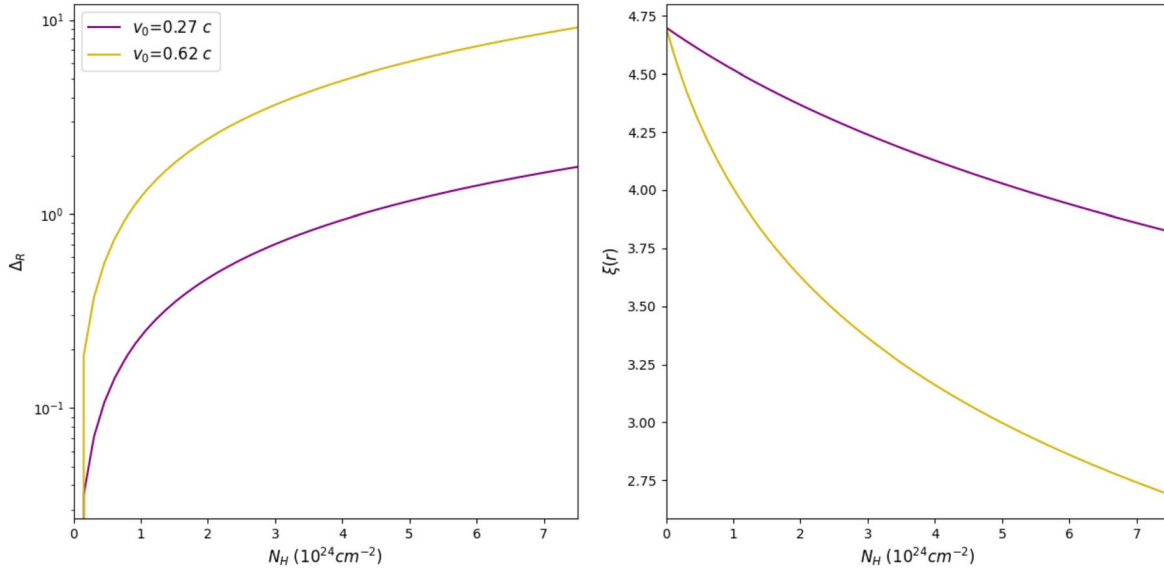


**Figure 11.** Scalings of the wind radial thickness and ionization parameter (left and right panel, respectively) for  $\log\left(\frac{\xi_0}{\text{erg cm s}^{-1}}\right) = 4.7$  and  $v_0 = 0.27c, = 0.62c$ , i.e., the best-fit velocity and the velocity inferred for the  $E = 14$  keV line (purple and yellow lines, respectively).

### Appendix D Analytical Constrains for $r_0$

In Section 3.2 we set a constraint for the launching radius of the wind  $r_0$  starting from geometrical considerations. In particular, we required a small radial thickness of the wind  $\Delta_r$  in order to obtain a reduced geometric dilution of the ionization parameter  $\xi(r)$  along the wind column. Using the best-fit values for the time-resolved spectra (see Table 4), we are now able to put updated constraints on  $r_0$ . For each time slice, the uncertainty associated with  $\xi_0$ <sup>13</sup> is given by its error bar; we define  $\xi_{\text{up}}, \xi_{\text{low}}$  as the maximum and minimum values at the 90% c.l. (as an example, for the 10 ks time slice  $\log\left(\frac{\xi_0}{\text{erg cm s}^{-1}}\right) = 4.6 \pm 0.6$ ; therefore,  $\log(\xi_{\text{up}}) = 5.2$ ,  $\log(\xi_{\text{low}}) = 4.0$ ).

Each value  $\xi_{\text{low}} \leq \xi_0 \leq \xi_{\text{up}}$  (together with the best-fit values  $N_{\text{H}}, v_0, \Gamma$ ) implies a different wind thickness. In fact, the gas density  $n$  can be derived as  $n = L'_{\text{ion}}/(\xi_0 r_0^2) = \left(\frac{1-v_0}{1\pm v_0}\right)^{\frac{2+\Gamma}{2}} \cdot L_{\text{ion}}/(\xi_0 r_0^2)$  (see Section 1), where  $L_{\text{ion}} = 2.67 \times 10^{43} \text{ erg s}^{-1}$ , as in the rest of the paper. Then, the wind outer boundary (i.e., the final radius) can be determined as  $r_{N_{\text{H}}} \equiv r(N_{\text{H}}) = r_0 + N_{\text{H}}/n$ , once assuming  $n$  as constant throughout the wind (see Section 3.2). Thus, as a result of the geometric dilution of the ionizing flux, the ionization parameter will range from  $\xi_0$  to  $\xi(r_{N_{\text{H}}})$ .

In order to obtain an order-of-magnitude estimate, we require the radial variation of  $\xi(r)$  to be comprised within the interval  $[\xi_{\text{low}}, \xi_{\text{up}}]$ . This can be expressed mathematically by requiring that when  $\xi_0 = \xi_{\text{up}}$ , then  $\xi(r_{N_{\text{H}}}) \geq \xi_{\text{low}}$ :

$$\begin{aligned} \xi(r_{N_{\text{H}}}) &= \frac{L'_{\text{ion}}}{n(r_{N_{\text{H}}})^2} = \xi_{\text{up}} \left( \frac{r_0}{r_{N_{\text{H}}}} \right)^2 \\ &= \xi_{\text{up}} \left( \frac{r_0}{r_0 + r_0^2 N_{\text{H}} \xi_{\text{up}} / L'_{\text{ion}}} \right)^2 \geq \xi_{\text{low}}, \end{aligned} \quad (\text{D1})$$

<sup>13</sup> We recall that  $\xi_0$  is defined as the ionization parameter  $\xi(r)$  for  $r = r_0$ , i.e., at the inner boundary of the wind.

**Table 6**  
Maximum Launching Radius  $r_{\text{max}}^0$  for Each Given Time Slice

| Time Frame (ks) | $r_{\text{max}}^0$ ( $r_S$ ) |
|-----------------|------------------------------|
| 10              | 1.2                          |
| 35              | 3.2                          |
| 130             | 3.3                          |
| 60 + 191        | 11.1                         |
| 202             | 4.9                          |
| 220             | 4.9                          |
| 278             | 0.2                          |
| 295             | 1.5                          |
| Mean            | 3.4                          |
| Median          | 3.2                          |

**Note.** The last two lines report the mean and median values, respectively.

which can be translated in the following condition for  $r_0$ :

$$r_0 \leq r_0^{\text{max}} = \frac{\sqrt{\xi_{\text{up}}/\xi_{\text{low}}} - 1}{N_{\text{H}} \xi_{\text{up}} / L'_{\text{ion}}}. \quad (\text{D2})$$

We report  $r_0^{\text{max}}$  for the different time slices in Table 6. We note that the average value is very close to our assumed  $r_0 = 5r_S$ , representing an important confirmation of our fitting strategy.

### ORCID iDs

Alfredo Luminari <https://orcid.org/0000-0002-1035-8618>  
 Andrea Marinucci <https://orcid.org/0000-0002-2055-4946>  
 Stefano Bianchi <https://orcid.org/0000-0002-4622-4240>  
 Barbara de Marco <https://orcid.org/0000-0003-2743-6632>  
 Chiara Feruglio <https://orcid.org/0000-0002-4227-6035>  
 Giorgio Matt <https://orcid.org/0000-0002-2152-0916>  
 Emanuele Nardini <https://orcid.org/0000-0001-9226-8992>  
 Enrico Piconcelli <https://orcid.org/0000-0001-9095-2782>  
 Simonetta Puccetti <https://orcid.org/0000-0002-2734-7835>

## References

- Alston, W. N., Fabian, A. C., Kara, E., et al. 2020, *NatAs*, **4**, 597
- Arnaud, K. A. 1996, in ASP Conf. Ser. 101: Astronomical Data Analysis Software and Systems V, ed. G. H. Jacoby & J. Barnes (San Francisco, CA: ASP), 17
- Astropy Collaboration, Price-Whelan, A. M., Sipőcz, B. M., et al. 2018, *AJ*, **156**, 123
- Astropy Collaboration, Robitaille, T. P., Tollerud, E. J., et al. 2013, *A&A*, **558**, A33
- Bianchi, S., Piconcelli, E., Chiaberge, M., et al. 2009, *ApJ*, **695**, 781
- Blandford, R. D., & Payne, D. G. 1982, *MNRAS*, **199**, 883
- Braito, V., Reeves, J. N., Severgnini, P., et al. 2021, *MNRAS*, **500**, 291
- Cash, W. 1976, *A&A*, **52**, 307
- Chartas, G., Cappi, M., Vignali, C., et al. 2021, *ApJ*, **920**, 24
- Costanzo, D., Dadina, M., Vignali, C., et al. 2022, *A&A*, **659**, A161
- Crenshaw, D. M., & Kraemer, S. B. 2012, *ApJ*, **753**, 75
- Crenshaw, D. M., Kraemer, S. B., & George, I. M. 2003, *ARA&A*, **41**, 117
- Cui, C., & Yuan, F. 2020, *ApJ*, **890**, 81
- Dannen, R. C., Proga, D., Kallman, T. R., & Waters, T. 2019, *ApJ*, **882**, 99
- Di Matteo, T., Springel, V., & Hernquist, L. 2005, *Natur*, **433**, 604
- Faucher-Giguère, C.-A., & Quataert, E. 2012, *MNRAS*, **425**, 605
- Ferland, G. J., Chatzikos, M., Guzmán, F., et al. 2017, *RMxAA*, **53**, 385
- Fiore, F., Feruglio, C., Shankar, F., et al. 2017, *A&A*, **601**, A143
- Fiore, F., Gaspari, M., Luminari, A., Tozzi, P., & De Arcangelis, L. 2023, arXiv:2304.12696
- Fukumura, K., Kazanas, D., Contopoulos, I., & Behar, E. 2010, *ApJ*, **715**, 636
- Gaspari, M., & Sadowski, A. 2017, *ApJ*, **837**, 149
- Gofford, J., Reeves, J. N., McLaughlin, D. E., et al. 2015, *MNRAS*, **451**, 4169
- Gofford, J., Reeves, J. N., Tombesi, F., et al. 2013, *MNRAS*, **430**, 60
- Guolo, M., Ruschel-Dutra, D., Grupe, D., et al. 2021, *MNRAS*, **508**, 144
- Guolo-Pereira, M., Ruschel-Dutra, D., Storchi-Bergmann, T., et al. 2021, *MNRAS*, **502**, 3618
- Harris, C. R., Millman, K. J., van der Walt, S. J., et al. 2020, *Natur*, **585**, 357
- Higginbottom, N., Proga, D., Knigge, C., et al. 2014, *ApJ*, **789**, 19
- Hopkins, P. F., & Elvis, M. 2010, *MNRAS*, **401**, 7
- Hunter, J. D. 2007, *CSE*, **9**, 90
- Igo, Z., Parker, M. L., Matzeu, G. A., et al. 2020, *MNRAS*, **493**, 1088
- Irwin, J. A., Schmidt, P., Damas-Segovia, A., et al. 2017, *MNRAS*, **464**, 1333
- Kaastra, J. S., Mewe, R., & Nieuwenhuijzen, H. 1996, in 11th Colloq. on UV and X-ray Spectroscopy of Astrophysical and Laboratory Plasmas, ed. K. Yamashita & T. Watanabe (Tokyo: Universal Academy Press), 411
- Kalberla, P. M. W., Burton, W. B., Hartmann, D., et al. 2005, *A&A*, **440**, 775
- Kallman, T., & Bautista, M. 2001, *ApJS*, **133**, 221
- Kara, E., Steiner, J. F., Fabian, A. C., et al. 2019, *Natur*, **565**, 198
- Keel, W. C. 1996, *ApJS*, **106**, 27
- King, A., & Pounds, K. 2015, *ARA&A*, **53**, 115
- Krongold, Y., Nicastro, F., Elvis, M., et al. 2007, *ApJ*, **659**, 1022
- Laurenti, M., Luminari, A., Tombesi, F., et al. 2021, *A&A*, **645**, A118
- Luminari, A., Nicastro, F., Elvis, M., et al. 2021, *A&A*, **646**, A111
- Luminari, A., Nicastro, F., Krongold, Y., Piro, L., & Linesh Thakur, A. 2022, arXiv:2212.01399
- Luminari, A., Piconcelli, E., Tombesi, F., et al. 2018, *A&A*, **619**, A149
- Luminari, A., Tombesi, F., Piconcelli, E., et al. 2020, *A&A*, **633**, A55
- Madsen, K. K., Fürst, F., Walton, D. J., et al. 2015, *ApJ*, **812**, 14
- Marinucci, A., Bianchi, S., Braito, V., et al. 2018, *MNRAS*, **478**, 5638
- Marinucci, A., Bianchi, S., Braito, V., et al. 2020, *MNRAS*, **496**, 3412
- Matzeu, G. A., Brusa, M., Lanzuisi, G., et al. 2023, *A&A*, **670**, A182
- Middei, R., Marinucci, A., Braito, V., et al. 2022, *MNRAS*, **514**, 2974
- Mingozzi, M., Cresci, G., Venturi, G., et al. 2019, *A&A*, **622**, A146
- Murphy, K. D., Yaqoob, T., & Terashima, Y. 2007, *ApJ*, **666**, 96
- Nardini, E., Reeves, J. N., Gofford, J., et al. 2015, *Sci*, **347**, 860
- Nicastro, F., Fiore, F., Perola, G. C., & Elvis, M. 1999, *ApJ*, **512**, 184
- Parker, M. L., Matzeu, G. A., Alston, W. N., et al. 2020, *MNRAS*, **498**, L140
- Parker, M. L., Pinto, C., Fabian, A. C., et al. 2017, *Natur*, **543**, 83
- Proga, D., Stone, J. M., & Kallman, T. R. 2000, *ApJ*, **543**, 686
- Protassov, R., van Dyk, D. A., Connors, A., Kashyap, V. L., & Siemiginowska, A. 2002, *ApJ*, **571**, 545
- Pudritz, R. E., Ouyed, R., Fendt, C., & Brandenburg, A. 2007, in Protostars and Planets V (Tucson, AZ: Univ. Arizona Press), 277
- Reeves, J. N., Braito, V., Nardini, E., et al. 2018, *ApJL*, **854**, L8
- Risaliti, G., Elvis, M., Fabbiano, G., Baldi, A., & Zezas, A. 2005, *ApJL*, **623**, L93
- Shakura, N. I., & Sunyaev, R. A. 1973, *A&A*, **24**, 337
- Tombesi, F., Cappi, M., Reeves, J. N., et al. 2010, *A&A*, **521**, A57
- Tombesi, F., Cappi, M., Reeves, J. N., et al. 2011, *ApJ*, **742**, 44
- Tombesi, F., Cappi, M., Reeves, J. N., & Braito, V. 2012, *MNRAS*, **422**, L1
- Tombesi, F., Meléndez, M., Veilleux, S., et al. 2015, *Natur*, **519**, 436
- Torrey, P., Hopkins, P. F., Faucher-Giguère, C.-A., et al. 2020, *MNRAS*, **497**, 5292
- Trippe, M. L., Crenshaw, D. M., Deo, R., & Dietrich, M. 2008, *AJ*, **135**, 2048
- Veilleux, S., Shopbell, P. L., & Miller, S. T. 2001, *AJ*, **121**, 198
- Walton, D. J., Middleton, M. J., Pinto, C., et al. 2016, *ApJL*, **826**, L26
- Walton, D. J., Risaliti, G., Harrison, F. A., et al. 2014, *ApJ*, **788**, 76
- Ward, M. J., Wilson, A. S., Penston, M. V., et al. 1978, *ApJ*, **223**, 788
- Yuan, F., & Narayan, R. 2014, *ARA&A*, **52**, 529
- Zappacosta, L., Piconcelli, E., Giustini, M., et al. 2020, *A&A*, **635**, L5
- Zubovas, K., & Nardini, E. 2020, *MNRAS*, **498**, 3633